Mindanao Dome variability over the last 160 kyr: Episodic glacial cooling of the West Pacific Warm Pool

Timothé Bolliet,[1] Ann Holbourn,[1] Wolfgang Kuhnt,[1] Carlo Laj,[2] Catherine Kissel,[2] Luc Beaufort,[3] Markus Kienast,[4] Nils Andersen,[5] and Dieter Garbe-Schönberg[1]

Received 29 March 2010; revised 10 December 2010; accepted 28 December 2010; published 26 February 2011.

[1] We present sea surface, upper thermocline, and benthic $\delta^{18}O$ data, as well as temperature and paleoproductivity proxy data, from the International Marine Global Change Study Program (IMAGES) Core MD06-3067 (6°31′N, 126°30′E, 1575 m water depth), located in the western equatorial Pacific Ocean within the flow path of the Mindanao Current. Our records reveal considerable glacial-interglacial and suborbital variability in the Mindanao Dome upwelling over the last 160 kyr. Dome activity generally intensified during glacial intervals resulting in cooler thermocline waters, whereas it substantially declined during interglacials, in particular in the early Holocene and early marine oxygen isotope stage (MIS) 5e, when upwelling waters did not reach the thermocline. During MIS 3 and MIS 2, enhanced surface productivity together with remarkably low SST and low upper ocean thermal contrast provide evidence for episodic glacial upwelling to the surface, whereas transient surface warming marks periodic collapses of the Mindanao Dome upwelling during Heinrich events. We attribute the high variability during MIS 3 and MIS 2 to changes in the El Niño Southern Oscillation state that affected boreal winter monsoonal winds and upper ocean circulation. Glacial upwelling intensified when a strong cyclonic gyre became established, whereas El Niño–like conditions during Heinrich events tended to suppress the cyclonic circulation, reducing Ekman transport. Thus, our findings demonstrate that variations in the Mindanao Dome upwelling are closely linked to the position and intensity of the tropical convection and also reflect far-field influences from the high latitudes.

Citation: Bolliet, T., A. Holbourn, W. Kuhnt, C. Laj, C. Kissel, L. Beaufort, M. Kienast, N. Andersen, and D. Garbe-Schönberg (2011), Mindanao Dome variability over the last 160 kyr: Episodic glacial cooling of the West Pacific Warm Pool, *Paleoceanography*, *26*, PA1208, doi:10.1029/2010PA001966.

1. Introduction

[2] The West Pacific Warm Pool (WPWP) plays a critical role within the ocean-climate system, as the accumulation of warm water in the western equatorial Pacific Ocean represents one of the main sources of moisture and heat for the mid to high latitudes. The WPWP is strongly affected by large-scale climatic features including the El Niño Southern Oscillation (ENSO) and the East Asian monsoon. Thus, the spatial and temporal evolution of the WPWP is closely linked to latitudinal oscillations in the mean position of the Intertropical Convergence Zone (ITCZ) and to changes in the equatorial Pacific surface ocean. Previous studies indicated that the WPWP showed considerable variability in the past and that some of the changes had major repercussions for global climate evolution [*Beaufort et al.*, 2001; *Stott et al.*, 2002, 2004, 2007; *Dannenmann et al.*, 2003; *Oppo et al.*, 2003; *Rosenthal et al.*, 2003; *Wang et al.*, 2004; *Thevenon et al.*, 2004; *Oppo and Sun*, 2005; *de Garidel-Thoron et al.*, 2001, 2007; *Zhang et al.*, 2007, 2009]. However, the temporal and spatial evolution of the WPWP remains the focus of vigorous debate and its long-term history is still poorly known. A major obstacle has been the difficulty in recovering continuous high-resolution sedimentary successions along the western Pacific coast, as the narrow continental shelf and strong prevailing currents generally inhibit long-term accumulation of sediments.

[3] Here, we present new Mg/Ca based paleotemperature reconstructions, stable isotope and paleoproductivity proxy data in a sedimentary core recovered in the central part of the WPWP within the flow path of the Mindanao Current. We measured stable isotope and Mg/Ca in two planktonic foraminifers living at different water depths within the upper water column. *Globigerinoides ruber* (sensu stricto white) is a near surface dweller, whereas *Pulleniatina obliquiloculata* reflects conditions within the upper thermocline [*Hemleben et al.*, 1989; *Ravelo and Fairbanks*, 1992; *Xu et al.*, 2006; *Farmer et al.*, 2007; *Cléroux et al.*, 2007; *Zuraida et al.*, 2009]. A consistent habitat depth at ~100 m for *P. obliquiloculata* is

[1]Institute of Geosciences, Christian-Albrechts University, Kiel, Germany.
[2]Laboratoire des Sciences du Climat et de l'Environnement/IPSL, CEA/CNRS/UVSQ, Gif-sur-Yvette, France.
[3]CEREGE, Aix-Marseille Université, CNRS, IRD, Europôle Méditerranéen de l'Arbois, Aix-en-Provence, France.
[4]Department of Oceanography, Dalhousie University, Halifax, Nova Scotia, Canada.
[5]Leibniz Laboratory for Radiometric Dating and Stable Isotope Research, Christian-Albrechts University, Kiel, Germany.

0883-8305/11/2010PA001966

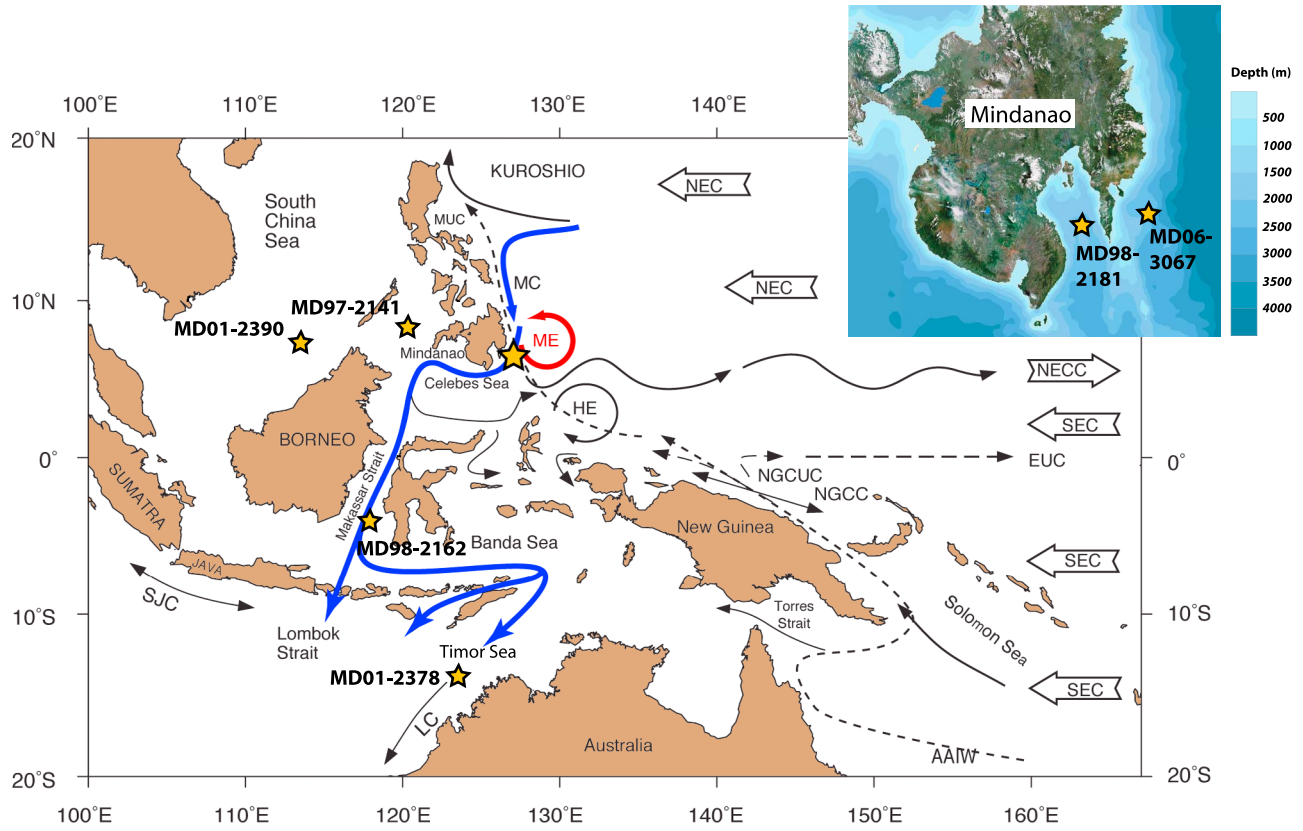

Figure 1. Location of Core MD06-3067 (orange star), bathymetry, and regional circulation in the Australasian area [modified from *Fine et al.*, 1994]. Solid blue lines indicate main path of Indonesian Throughflow. Red circular arrow indicates Mindanao Eddy generating Mindanao Dome. NEC is North Equatorial Current, NECC is North Equatorial Counter Current, SEC is South Equatorial Current, EUC is Equatorial Undercurrent, NGCC is New Guinea Coastal Current, NGCUC is New Guinea Coastal Undercurrent, MUC is Mindanao Undercurrent, AAIW is Antarctic Intermediate Water, SJC is South Java Current, LC is Leeuwin Current, MC is Mindanao Current, ME is Mindanao Eddy, and HE is Halmahera Eddy. Positions of cores discussed in this study are also shown: Core MD97-2141 [*de Garidel-Thoron et al.*, 2001; *Dannenmann et al.*, 2003; *Oppo et al.*, 2003; *Rosenthal et al.*, 2003], Core MD01-2390 [*Steinke et al.*, 2010], Core MD98-2181 [*Stott et al.*, 2002; *Saikku et al.*, 2009], Core MD98-2162 [*Visser et al.*, 2003], and Core MD01-2378 [*Xu et al.*, 2006, 2010].

supported by Mg/Ca–derived temperature estimates and by calculation of calcification temperatures from $\delta^{18}O_{carbonate}$ and $\delta^{18}O_{seawater}$ measurements in the Timor Sea, which closely match regional WOA05 annual average temperature at 100 m water depth [*Locarnini et al.*, 2006; *Zuraida et al.*, 2009]. Furthermore, a habitat depth of 60–80 m was estimated for *P. obliquiloculata* in the upwelling area off South Java [*Mohtadi et al.*, 2009], indicating that habitat depth does not change significantly under upwelling conditions.

[4] Core MD06-3067 is located at a water depth of 1575 m in the open western Pacific Ocean (6°31′N, 126°30′E), approximately 45 km east of Mindanao Island (Figure 1) [*Laj et al.*, 2006]. This 15.5 m long sediment core provides a unique opportunity to closely track past variations of the upper water column in a highly sensitive part of the WPWP, and in particular to relate regional hydrological changes to the activity of the Mindanao Current (MC), SE Asian climate evolution and high-latitude climate variability over the last 160 kyr.

2. Regional Oceanography and Climate

[5] The Pacific North Equatorial Current (NEC) contributes to the zonal transfer of heat across the Pacific Ocean, and therefore influences the short- and long-term variability of the WPWP. Today, the NEC splits into two branches near the eastern coast of the Philippine islands (15°N) [*Toole et al.*, 1990]. The northern branch eventually forms the main part of the Kuroshio Current, whereas the southern branch gives rise to the MC, which transfers waters in the upper 300 m along the southeastern coast of the Philippine islands, and ultimately contributes to the Indonesian Throughflow (ITF) transport (Figure 1).

[6] East of Mindanao Island, a stationary eddy (Mindanao Eddy, centered at 7°N, 130°E and measuring 200 to 300 km

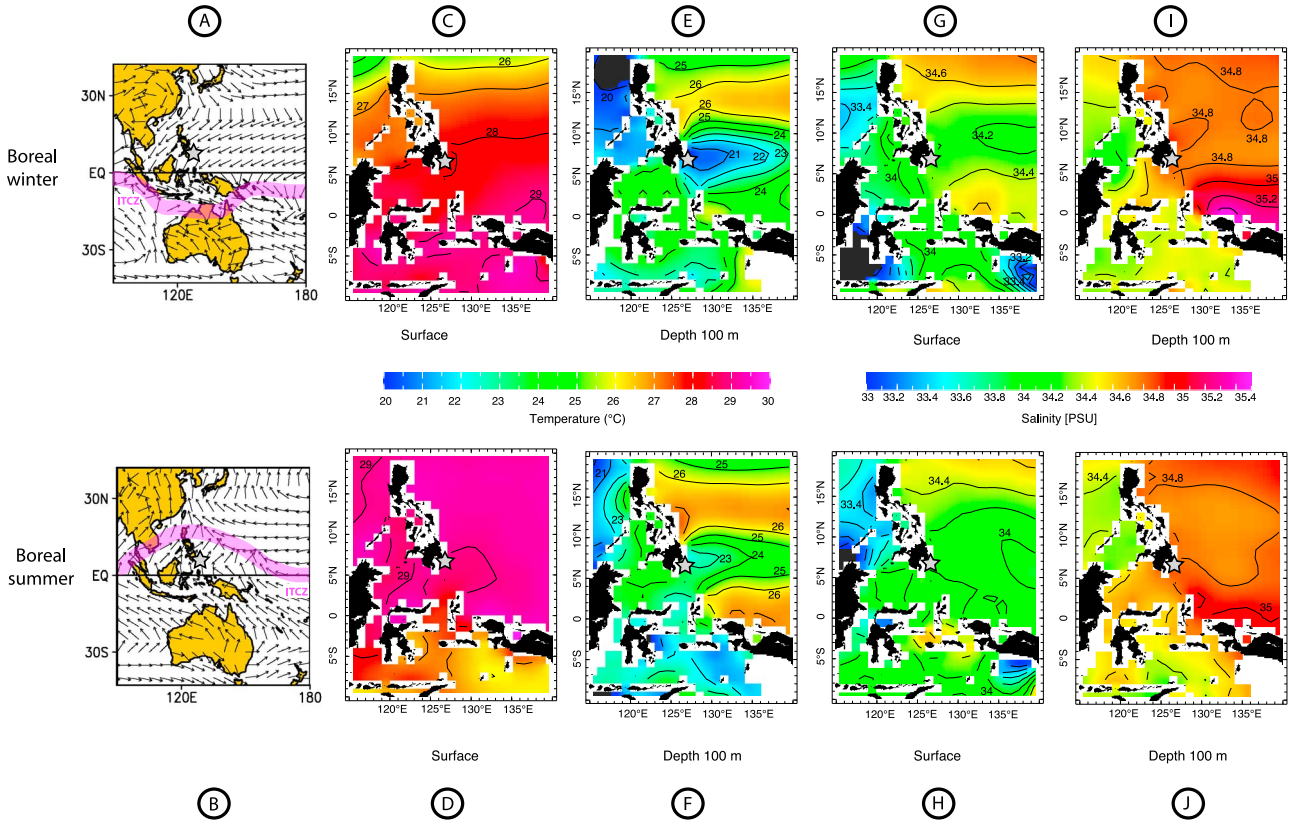

Figure 2. Climatology of the Australasian region. (a) Surface winds direction during boreal winter (January), averaged from 1948 to 2010 (modified from NCEP/NCAR Reanalysis Project, NOAA/ESRL Physical Sciences Division) [*Kalnay et al.*, 1996]. Pink shading indicates winter position of ITCZ. Grey star marks position of Core MD06-3067. (b) Surface winds during boreal summer (July), averaged from 1948 to 2010. Note reversal of trade winds over core location and northward shift of ITCZ position during boreal summer. (c) SST during boreal winter (January–March) [*Locarnini et al.*, 2006]. (d) SST during boreal summer (July–September) [*Locarnini et al.*, 2006]. (e) Thermocline (100 m depth) temperature during boreal winter (January–March) [*Locarnini et al.*, 2006]. Note cold sector east of Mindanao Island due to Mindanao Dome. (f) Thermocline (100 m depth) temperature during boreal summer (July–September) [*Locarnini et al.*, 2006]. Note reduced cold area east of Mindanao Island due to decrease in Mindanao Dome activity during boreal summer. (g) Sea surface salinity during boreal winter (January–March) [*Antonov et al.*, 2006]. Grey star marks position of Core MD06-3067. (h) Sea surface salinity during boreal summer (July–September) [*Antonov et al.*, 2006]. (i) Thermocline (100 m depth) salinity during boreal winter (January–March) [*Antonov et al.*, 2006]. Note insignificant impact of Mindanao Dome on local thermocline salinity. (j) Thermocline (100 m depth) salinity during boreal summer (July–September) [*Antonov et al.*, 2006].

in diameter; Figure 1), is embedded in the regional circulation system, and is characterized by seasonal midgyre upwelling [*Takahashi*, 1959; *Masuzawa*, 1968; *Lukas*, 1988; *Lukas et al.*, 1991; *Masumoto and Yamagata*, 1991; *Gordon and McClean*, 1999; *Qu et al.*, 1999; *Tozuka et al.*, 2002; *Firing et al.*, 2005]. This cyclonic feature, which is mainly driven by the MC, engenders local and seasonal upwelling. Oceanographic observations indicate that upwelled waters are present up to 75 m water depth, but do not reach the surface [*Udarbe-Walker and Villanoy*, 2001; *Tozuka et al.*, 2002], thus, forming a dome (Mindanao Dome) rather than upwelling sensu stricto (Figure 2). The Mindanao Dome is characterized by strong seasonality, as shown by oceanographic observations indicating that dome activity increases markedly during winter [*Toole et al.*, 1990; *Masumoto and Yamagata*, 1991; *Wijffels et al.*, 1995]. The origin and dynamics of the Mindanao Eddy, which induces the Mindanao Dome, are still poorly known. Some studies indicate that changes in the ITCZ position and East Asian winter monsoon variability are the main factors controlling this cyclonic feature [*Masumoto and Yamagata*, 1991; *Tozuka et al.*, 2002].

[7] The area south and east of Mindanao is affected by monsoonal variability with marked seasonality in the position of the ITCZ driving local wind and rainfall patterns (Figures 2a and 2b), even though there is no true dry/wet season due to the relative high amount of precipitation

falling over this area during the whole year [*Rudolf et al.*, 2010]. This may explain the small amplitude in salinity change of surface and thermocline waters between summer and winter (Figures 2g–2j). Early and late boreal summer are the most humid seasons, whereas precipitation is reduced by ~50% during boreal winter and spring. Seasonality is also evident in wind stress data, with stronger winds during boreal summer and winter compared to spring and fall: west to southwest winds are dominant from June to September, whereas east to northeast winds blow from December to March (Figures 2a and 2b).

[8] The Mindanao region is also influenced by ENSO, with El Niño events marked by clear decreases in rainfall, due to eastward migration of the convection and precipitation cells over the Pacific basin [*Lyon et al.*, 2006]. In contrast, La Niña periods are characterized by enhanced precipitation over the western equatorial Pacific Ocean and surrounding land areas. ENSO is also reflected by changes in the seasonal wind pattern, as boreal winter monsoonal winds are weaker during El Niño events and boreal summer monsoonal winds decrease during La Niña periods [*Wang et al.*, 2000; *Sakai and Kawamura*, 2009].

3. Material and Methods

[9] International Marine Global Change Studies Program (IMAGES) Core MD06-3067 (6°31′N, 126°30′E, 1575 m water depth) was recovered with the Calypso Giant Piston Corer on board R/V *Marion-Dufresne* during the IMAGES cruise "Marco Polo 2" in June 2006 [*Laj et al.*, 2006]. The core is 15.53 m long and consists mainly of homogenous dark olive gray, silty clay, except for the upper two meters that are composed of brown to olive gray silty clay.

3.1. Sampling Strategy

[10] Core MD06-3067 was initially sampled at 10 cm intervals equivalent to ~1 kyr time resolution (155 samples of 1 cm thickness, equivalent to ~40 cc) for planktonic and benthic stable isotopes and Mg/Ca analysis. The younger part of the core (MIS 4 to Holocene) was subsequently sampled at 2 cm (~200 years time resolution) intervals. Samples were dried, weighed, then washed over a 63 μm sieve. Residues were dried on a sheet of filter paper, then weighed and sieved into 63–150 μm, 150–250 μm, 250–315 μm and >315 μm fractions. About 15–50 tests of the planktonic foraminifer *G. ruber* (sensu stricto white) and 10–40 tests of the upper thermocline dweller *P. obliquiloculata* were picked from the 250–315 μm size fraction. For the initial analysis, 10–20 specimens were selected for stable isotope analysis and 10–20 (*P. obliquiloculata*) and 20–30 (*G. ruber*) specimens for Mg/Ca measurement. For the high-resolution analysis, all foraminifers were crushed together, then divided into aliquots for stable isotope and Mg/Ca analyses. In rare occasions, when the number of tests was low, we analyzed foraminifers from an adjacent sample, equivalent to a 2 cm thick interval. For benthic isotopes, 3–5 specimens of *Planulina wuellerstorfi* and/or *Cibicidoides mundulus* were selected from the >250 μm size fraction, except in a few samples where only 1–2 specimens were available. In rare occasions where neither of these species was present, we analyzed *Uvigerina proboscidea*, then deducted 0.64‰ from the δ^{18}O values, as suggested by *Shackleton and Opdyke* [1973].

3.2. Stable Isotopes

[11] All samples were gently crushed into large fragments, agitated in ethanol for 2–3 s in an ultrasonic bath, decanted, then dried at 40°C. Stable carbon and oxygen isotopes were measured with a Finnigan MAT 251 mass spectrometer at the Leibniz Laboratory, Kiel University. The system is coupled online to a Carbo-Kiel Device (Type I) for automated CO_2 preparation from carbonate samples for stable isotopic analysis. Samples were reacted by individual acid addition (99% H_3PO_4 at 73°C). Standard external error is better than ±0.07‰ for δ^{18}O as documented by the performance of international and laboratory-internal carbonate standard materials. Replicate δ^{18}O measurements on 70 samples of *G. ruber* and on 76 samples of *P. obliquiloculata* indicate external reproducibility of ±0.10‰ and ±0.12‰, respectively. Replicate δ^{18}O measurements on 31 samples of benthic foraminifers show an external reproducibility of ±0.07‰.

3.3. Radiocarbon Dating

[12] For accelerator mass spectrometry (AMS) ^{14}C dating, about 900–1500 well-preserved tests of the planktonic foraminifer *G. ruber* were picked from the >250 μm size fraction in samples between 10 and 420 cm. In two samples (KIA 33257, 11cm, and KIA 33790, 210 cm), where the abundance of this species was low, we analyzed *Globigerinoides sacculifer* and *G. ruber* together. In one sample (KIA 33258, 60 cm), we analyzed mixed planktonic species, due to low numbers of *G. sacculifer* and *G. ruber*. AMS^{14}C dating was performed at the Leibniz laboratory, Kiel University, following the protocol described by *Nadeau et al.* [1997] and *Schleicher et al.* [1998]. For samples younger than 13 ka, a reservoir age of 480 years was subtracted from the conventional ages before conversion to calendar ages. For older samples, we applied a reservoir age of 630 years following *Saikku et al.* [2009]. Conventional ages were converted to calendar ages following the protocol established by *Fairbanks et al.* [2005].

3.4. Mg/Ca Analysis

[13] Foraminifers were weighed with an ultraprecision balance (Sartorius ME5 OCE, repeatability ±1 μg, linearity ±4 μg), gently crushed to expose inner chamber walls, then put into vials for cleaning. The cleaning procedure used for removing contaminant phases includes oxidative and reductive steps following methods outlined by *Martin and Lea* [2002]. Prior to analysis, full dissolution of the test fragments was obtained with 1 mL 0.1 N nitric acid and ultrasonication, and aliquots were diluted in such a way that the final solution contained ~50 (25–75) mg L^{-1} Ca. Only freshly prepared subboiled HNO_3 was used and all work was done in class100 clean benches. The dissolved samples were analyzed on a radial viewing simultaneous ICP-OES (Spectro Ciros SOP CCD, Spectro Analytical Instruments, Germany) at the Institute of Geosciences, Kiel University, applying an intensity-calibration method [*de Villiers et al.*, 2002] and bracketing standards. Batches of 6 unknown samples were bracketed by a synthetic normalization standard. At least 10%

of unknown samples were replicate measurements of samples analyzed hours before, or during previous day analytical sessions. Typical external error is 0.1% rel. (1-sigma) for Mg/Ca. Carbonate certified reference material (ECRM 752–1, BAM RS3) [*Greaves et al.*, 2008] was analyzed for monitoring analytical accuracy. Matrix effects caused by the easily ionizable element Ca were investigated and found to be negligible. Samples with a recovery in Ca concentration of less than 20% were rejected. Fe/Ca, Al/Ca and Mn/Ca ratios were additionally monitored to test cleaning efficiency, and samples showing a significant correlation between Fe/Ca, Al/Ca, Mn/Ca and Mg/Ca values were excluded, following *Schmidt et al.* [2004]. Replicate measurements of 66 samples of *G. ruber* and 39 samples of *P. obliquiloculata* (measured two to four times) indicated relative standard deviation of 0.18 and 0.11 mmol/mol, which is equivalent to a SST deviation of ±0.48 and ±0.52°C, respectively.

[14] Foraminiferal Mg/Ca ratios were then converted into temperatures using the equations of *Anand et al.* [2003] that provide an accuracy of ±1.2°C in estimating calcification temperature (T in °C):

$$\mathrm{Mg/Ca} = 0.38(\pm 0.02)\ \exp\ 0.090(\pm 0.003)\ \mathrm{T\ for}\ \textit{G. ruber}$$

and

$$\mathrm{Mg/Ca} = 0.328(\pm 0007)\ \exp\ 0.090(\pm 0.003)\ \mathrm{T\ for}\ \textit{P. obliquiloculata}.$$

The equation for *G. ruber* (350–500 microns) was previously used in other regional studies, and gives similar results as the equation of *Dekens et al.* [2002] without dissolution correction. We applied no correction for the reductive step included in our cleaning protocol, which generally results in a small decrease in Mg/Ca leading to temperature underestimation of up to 0.6°C [*Rosenthal et al.*, 2004]. *Bian and Martin* [2010] validated the use of a reductive step in the cleaning procedure for Mg/Ca analysis, and demonstrated the potential of reductive cleaning to improve the Mg/Ca data.

[15] Carbonate dissolution is unlikely to have affected the Mg/Ca ratio of our samples due to the relatively shallow water depth of 1575 m of Site MD06-3067. Nonetheless, potential effects of carbonate dissolution on Mg/Ca were monitored by comparing average weights of individual shells of *G. ruber* (201 samples) and *P. obliquiloculata* (190 samples) with Mg/Ca data obtained from the same samples. Shell weights of *G. ruber* remain relatively constant throughout, while *P. obliquiloculata* shells exhibit more variability in weight (Figure S2 in the auxiliary material).[1] Yet, systematic variations are not observed and there is no correlation between shell weights and Mg/Ca ratios (Figures S2a and S2b). We use this as an indication that our Mg/Ca data were not affected by carbonate dissolution. Peak occurrence of benthic foraminifers with extremely fragile, thin-walled tests (globobulimids) in intervals, where Mg/Ca is episodically low, further indicates that carbonate dissolution is not a cause of Mg loss. Although the deeper dweller *P. obliquiloculata* exhibits more variability in individual shell weight, no significant link with cold/warm phases is detected.

[1] Auxiliary materials are available in the HTML. doi:10.1029/2010PA001966.

3.5. Calculation of $\delta^{18}O_{sw}$

[16] We calculated surface and thermocline seawater $\delta^{18}O$ composition ($\delta^{18}O_{sw}$ versus V-SMOW) from paired Mg/Ca and $\delta^{18}O$ measurements of *G. ruber* and *P. obliquiloculata*, respectively. For this we used the equation of *Bemis et al.* [1998]:

$$\delta^{18}O_{sw} = 0.27 + \big(T(^{\circ}C) - 16.5 + 4.8 \times \delta^{18}O(V-PDB)\big)/4.8.$$

A core top $\delta^{18}O_{sw}$ value of 0.07‰ was calculated for surface water from an average of the last three Holocene measurements in Core MD06-3067. This value is in agreement with the regional average of 0.1‰, in the global $\delta^{18}O_{sw}$ database [*LeGrande and Schmidt*, 2006].

[17] A modern $\delta^{18}O_{sw}$ value of 0.39‰ for thermocline water was calculated from the salinity value at 100 m water depth at the location of Core MD06-3067 (34.9 psu) [*Antonov et al.*, 2006] using the empirical relation by *Fairbanks et al.* [1997]:

$$\delta^{18}O_{sw} = +0.273 \times S - 9.14,$$

where S is the salinity (psu) and $\delta^{18}O_{sw}$ is expressed in per mil (‰) relative to VSMOW. The $\delta^{18}O_{sw}$ value of 0.27‰ that we derive from paired late Holocene *P. obliquiloculata* $\delta^{18}O$ and Mg/Ca agrees well with the estimated water column $\delta^{18}O_{sw}$ value, and supports the upper thermocline habitat depth of this species.

[18] A correction for relative past changes in sea level on the $\delta^{18}O_{sw}$ of the global ocean [after *Waelbroeck et al.*, 2002] was applied to the surface and thermocline $\delta^{18}O_{sw}$ records of Core MD06-3067.

3.6. Seasonality of Sea Surface and Upper Thermocline Proxies

[19] Sediment trap data indicate a peak of *G. ruber* fluxes during the summer months in the Panama Basin [*Thunell and Reynolds*, 1984]. Combined sediment trap and plankton tow studies in the South China Sea also show higher percentage abundances of *G. ruber* during the summer months, while total fluxes are enhanced during the boreal winter monsoon, suggesting that the seasonality of *G. ruber* is less pronounced than for other surface dwelling species such as *G. sacculifer* [*Lin et al.*, 2004; *Lin and Hsieh*, 2007]. A recent study within the monsoon driven South Java upwelling [*Mohtadi et al.*, 2009] indicates a similar seasonality of flux rates for *G. ruber* and *P. obliquiloculata*. Flux rates of both species are less influenced by upwelling seasonality than typical upwelling indicators such as *G. bulloides*, *G. glutinata* and *N. pachyderma* (dextral).

3.7. Paleoproductivity Proxies

3.7.1. Coccoliths

[20] We sampled Core MD06-3067 for coccolith counts at 10 cm intervals (155 samples), corresponding to a temporal

resolution of ~1 kyr. A few milligrams of sediment were evenly spread on a glass slide, then 40 digital photos were taken for each slide with a camera mounted on a Leica DMRBE transmitted light microscope with a 50X oil immersion objective. Counting of coccoliths was performed with an automated system of coccolith recognition (SYRACO, Système de Reconaisance Automatique de Coccolithes) using a neural network algorithm (see details in the works by *Dollfus and Beaufort* [1999] and *Beaufort and Dollfus* [2004]). A total of 14 taxa were identified, of which six represent an average of 89% of the total assemblage: *Emiliania huxleyi*, *Florisphaera profunda*, *Gephyrocapsa ericsonii*, *Gephyrocapsa muellerae*, *Gephyrocapsa oceanica* and *Helicosphaera* spp. Within these taxa, the average number of coccoliths recognized by the system is ~1600 specimens before visual correction and ~1100 specimens after correction. Primary productivity was estimated using the equation of *Beaufort et al.* [1997], based on the empirical relationship between the relative abundances of *F. profunda* and productivity:

$$PP = 617 - [279 \times \log(Fp + 3)].$$

where PP is the primary productivity and Fp is the relative abundance of *F. profunda*. This equation was established by comparing Indian Ocean core top data with modern productivity based on satellite chlorophyll, and is considered representative for the Pacific Ocean [*Beaufort et al.*, 2001].

3.7.2. Benthic Foraminifers

[21] Benthic foraminifers were picked and counted in the size fraction >250 μm from 111 samples (10 or 20 cm intervals). In samples, where benthic foraminiferal abundance was high, a quantitative split was picked, and census counts were then reconverted to whole samples. Numbers of benthic foraminifers picked per sample generally vary between 150 and 600 (average of 348) specimens except in rare samples, where foraminiferal abundance was low and fewer specimens were picked. We used percentage abundances of four main groups that are indicative of high and intermediate carbon export flux to the seafloor [*Kuhnt et al.*, 1999; *Holbourn et al.*, 2005]. Counts of globocassidulinids include *Globocassidulina subglobosa* and *G. elegans*. Globobuliminids include *Globobulimina pupoides*, *G. ovata*, *G. pyrula* and *G. pacifica*. Miliolids include *Pyrgo murrhina*, *P. serrata* and *Pyrgo* spp. *Bolivinita quadrilatera* is a mesotrophic indicator species that shows marked variations in abundance in Core MD06-3067.

4. Results

4.1. Chronology

[22] The benthic δ^{18}O record from Core MD06-3067 indicates recovery of a complete succession from the Holocene down to MIS 6 (Figures 3a and 3b). Interglacial MIS 5e and MIS 1 and glacial periods (MIS 6 and MIS 2) as well as Antarctic warm events A1–A4 (between 38 and 58 ka BP) can be clearly identified. The age model is based on seven AMS^{14}C dates in the upper part of the core (11–420 cm) and on correlation of the benthic δ^{18}O between 253 and 1550 cm in Core MD06-3067 with the δ^{18}O record from the EPICA Dronning Maud Land ice core (EDML1 chronology) [*Ruth et al.*, 2007]. AMS^{14}C dates and tie points used to derive the age model are given in Table 1 and shown in Figure 3.

[23] AMS^{14}C dates at 260 and 280 cm (samples KIA 35211 and KIA 35212; Table 1) were not used because ages for surface water appear influenced by upwelling of deeper, older water during the last glacial period. These two AMS^{14}C dates are older by ~1800 and ~3000 years, respectively, than ages derived from our age model (Figure 3). *Stott et al.* [2007] and *Saikku et al.* [2009] suggested that the benthic δ^{18}O signal in a nearby location within the Mindanao embayment (Core MD98-2181; Figure 1) records Antarctic climate variations with a delay of ~1000 years. To maintain coherency with these studies, we removed 1000 years from the ages that were derived from graphical correlation of benthic δ^{18}O with the δ^{18}O record from the EPICA ice core.

[24] An interpolated curve was fitted through the δ^{18}O tie points and AMS^{14}C data points using a Stineman function (Smooth function in KaleidaGraph). This function fits a curve that passes through the data points and matches the slopes at these points. The output of the function then has a geometric weight applied to the current point and ±10% of the data range. The resulting smoothed curve was then sampled at relevant intervals. The age model in the lower part of the core (1335–1550 cm corresponding to MIS 6) is based on linear extrapolation from the lowest tie point (onset of Termination II at 1335 cm) to the base of the core, assuming a constant sedimentation rate of 10 cm/kyr, which is consistent with glacial sedimentation rates during MIS 2.

[25] The Laschamp geomagnetic excursion was used to test the robustness of our age model. This event is centered at ~511 cm in Core MD06-3067 (C. Laj et al., manuscript in preparation, 2011), which corresponds in our age model to ~40.8 ka. This is consistent with the radiometric age of 40.4 ± 2 ka (2s) obtained from the lava flow at the Laschamp locality [*Guillou et al.*, 2004] and more recently refined to 40.7 ± 0.95 ka (2s) [*Singer et al.*, 2009]. The relative position of the Laschamp event (40.8 ka) and Heinrich event H4 (39.8–38.5 ka) in our record (Figure 3b) also agrees with the GICC05 ice core chronology [*Svensson et al.*, 2008].

[26] Sedimentation rates remain relatively constant, with an average rate of 10 cm/kyr, except within the upper two meters of the core, where the rate increases to 35 cm/kyr (Figure 3a). This higher apparent rate is due to the piston coring system, as illustrated by the vertical alignment of magnetic particles [*Kissel et al.*, 2010], which can cause expansion of the upper core section and on occasion causes oversampling (i.e., lateral sediment intake) in the upper part of the core [*Széréméta et al.*, 2004].

4.2. Benthic δ^{18}O

[27] The benthic oxygen isotope record shows glacial-interglacial fluctuations with amplitudes of ~1.7‰ over both Terminations I and II (from 4.1 to 2.4‰ for Termination II and from 4.2 to 2.5‰ for Termination I; Figure 3b). The values of δ^{18}O fluctuate between 3.2 and 4‰ during MIS 3, and reach 3.8‰ during MIS 4, which is 0.8‰ more than for MIS 5a. The main MIS 5 substages a–e can be identified, as well as Antarctic warm events AIM4 and A1–4 (at ~29, 39, 46, 53 and 59 ka; Figure 3b).

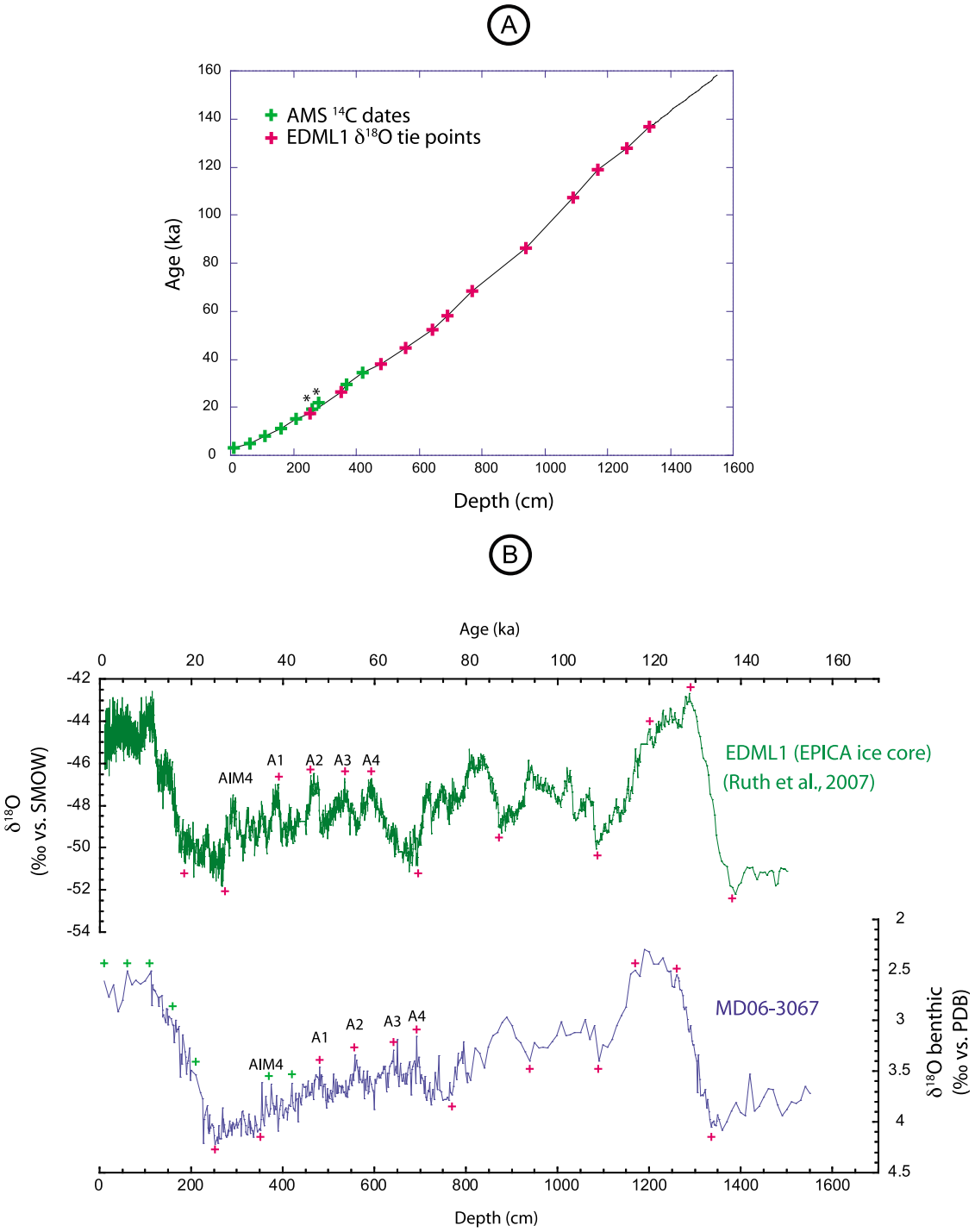

Figure 3. Age model based on seven accelerator mass spectrometry (AMS) ^{14}C dates and 12 $\delta^{18}O$ events for Core MD06-3067 (Table 1). (a) Depth/age plot with AMS^{14}C dates (green crosses) and $\delta^{18}O$ events (pink crosses). Asterisks mark AMS^{14}C dates not used for age model. (b) Comparison of MD06-3067 benthic $\delta^{18}O$ signal (bottom curve) with EDML1 $\delta^{18}O$ (top curve) [*Ruth et al.*, 2007]. Green crosses indicate AMS^{14}C dates. Pink crosses indicate $\delta^{18}O$ events used as tie points. AIM4 and A1 to A4 refer to Antarctic Isotope Maxima or warm events.

Table 1. Planktonic Foraminiferal AMS^{14}C Dates and Benthic δ^{18}O Events Used to Derive the Age Model for Core MD06-3067[a]

Type	Depth (cm)	Calendar Age (years BP)	Description
AMS^{14}C date	11 (section 1; 11–12 cm)	3390 ± 27	Species analyzed: *G. ruber, G. sacculifer*. ^{14}C conventional age: 3655 ± 30 years. Reservoir age correction: 480 years. Reference: KIA 33257.
AMS^{14}C date	60 (section 1; 60–61 cm	4750 ± 70	Species analyzed: mixed surface dwelling planktonic foraminifers. ^{14}C conventional age: 4655 ± 30 years. Reservoir age correction: 480 years. Reference: KIA 33258.
AMS^{14}C date	110 (section 1; 110–111 cm)	8205 ± 49	Species analyzed: *G. ruber*. ^{14}C conventional age: 7870 ± 40 years. Reservoir age correction: 480 years. Reference: KIA 33788.
AMS^{14}C date	160 (section 2; 10–11 cm)	11,010 ± 125	Species analyzed: *G. ruber*. ^{14}C conventional age: 10100 ± 45 years. Reservoir age correction: 480 years. Reference: KIA 33789.
AMS^{14}C date	210 (section 2; 60–61 cm)	15,250 ± 124	Species analyzed: *G. ruber, G. sacculifer*. ^{14}C conventional age: 13725 ± 65 years. Reservoir age correction: 630 years. Reference: KIA 33790.
δ^{18}O event	253 (section 2; 103–104 cm)	(18,400) 17400	Onset of Termination I
AMS^{14}C date	260 (section 2; 110–111 cm)	19,460 ± 103	Species analyzed: *G. ruber*. ^{14}C conventional age: 16970 +90/−80 years. Reservoir age correction: 630 years. Reference: KIA 35211. Not used for generating age model.
AMS^{14}C date	280 (section 2; 130–131 cm)	22,100 ± 131	Species analyzed: *G. ruber*. ^{14}C conventional age: 19110 ± 100 years. Reservoir age correction: 630 years. Reference: KIA 35212. Not used for generating age model.
δ^{18}O event	352 (section 3; 52–53 cm)	(27,300) 26,300	Benthic δ^{18}O increase at end of MIS 3
AMS^{14}C date	370 (section 3; 70–71 cm)	29,690 ± 313	Species analyzed: *G. ruber*. ^{14}C conventional age: 25410 +190/−180 years. Reservoir age correction: 630 years. Reference: KIA 35214.
AMS^{14}C date	420 (section 3; 120–121 cm)	34,470 ± 339	Species analyzed: *G. ruber*. ^{14}C conventional age: 29690 +300/−290 years. Reservoir age correction: 630 years. Reference: KIA 35215.
δ^{18}O event	480 (section 4; 30–31 cm)	(39,000) 38,000	Lowest δ^{18}O value at onset of A1 plateau
δ^{18}O event	557 (section 4; 107–108 cm)	(45,900) 44,900	End of A2 event
δ^{18}O event	642 (section 5; 42–43 cm)	(53,500) 52,500	Lowest δ^{18}O value of A3 plateau
δ^{18}O event	692 (section 5; 92–93 cm)	(59,200) 58,200	Lowest δ^{18}O value in center of A4 plateau
δ^{18}O event	769 (section 6; 19–20 cm)	(69,400) 68,400	Onset of MIS4
δ^{18}O event	939 (section 7; 39–40 cm)	(87,100) 86,100	End of MIS 5b
δ^{18}O event	1089 (section 8; 39–40 cm)	(108,500) 107,500	End of MIS 5d
δ^{18}O event	1169 (section 8; 119–120 cm)	(120,000) 119,000	End of MIS 5e plateau
δ^{18}O event	1260 (section 9; 60–61 cm)	(128,800) 127,800	Onset of MIS 5e plateau
δ^{18}O event	1335 (section 9; 135–136 cm)	(137,900) 136,900	Onset of Termination II

[a]Calendar ages of δ^{18}O events in EDML1 (EPICA ice core) [*Ruth et al.*, 2007] are given in parentheses. Ages of δ^{18}O events in Core MD06-3067 were shifted by 1000 years to accommodate signal propagation time from the Southern Ocean to the location of Core MD06-3067. For discussion, see text.

4.3. Planktonic δ^{18}O, Temperature, and $\delta^{18}O_{sw}$ Reconstructions

4.3.1. *G. ruber* and *P. obliquiloculata* δ^{18}O

[28] The surface and thermocline δ^{18}O records (Figures 4a and 5a) from MIS 6 to the late Holocene exhibit well-defined main isotopic stages with overall higher variability in the thermocline than in the surface signal. The MIS 5e plateau at 118–127 ka is clearly defined in the *G. ruber* record, with values ranging from −2.5 to −2.6‰. The thermocline signal exhibits the highest depletion (−1.3 to −1.4‰) during MIS 5e (between 120 and 124 ka). The transition between MIS 5e to 5d corresponds to an enrichment of ~0.6‰ and ~0.9‰ in surface and thermocline δ^{18}O values, respectively. During the remainder of MIS 5, the δ^{18}O contrast between cold (5b and d) and warm (5a and c) phases is higher in the *P. obliquiloculata* thermocline record than in the surface record. The cold MIS 4 interval is marked by an enrichment of 0.6‰ in *G. ruber* δ^{18}O and 0.25 to 0.4‰ in *P. obliquiloculata* δ^{18}O, whereas the transition between MIS 4 and 3 appears as a sudden depletion of 0.3‰ in both records. During MIS 2 and MIS 6, δ^{18}O values of surface and thermocline waters are similar as well as the amplitude of the decreases (~1.6‰) over Termination I (18.5–11 ka) and Termination II (137–127 ka). In the Holocene, average δ^{18}O values for both surface and upper thermocline waters are close to MIS 5e values.

4.3.2. Sea Surface and Thermocline Temperature

[29] Temperature reconstructions based on Mg/Ca analysis of *G. ruber* and *P. obliquiloculata* in Core MD06-3067 indicate substantial glacial-interglacial temperature contrasts (Figures 4b and 5b). The last deglaciation is marked by a warming of 5°C in both surface and thermocline waters, whereas the amplitude of warming during Termination II is larger in thermocline waters (5°C) than in surface waters (3.5°C). The higher amplitude of surface warming during Termination I results from the ~2°C colder SST during MIS 2 compared to MIS 6 (average of 24.5°C for MIS 2 in contrast to 26.5°C for MIS 6). The offset in SST between MIS 2 and MIS 6 is contrasted by surface δ^{18}O at MD06-3067 that is similar for MIS 2 and MIS 6, possibly indicating an influence of $\delta^{18}O_{sw}$ and salinity.

[30] During MIS 5e, the *P. obliquiloculata* temperature record exhibits a sharp maximum around 126 ka, which is contrasted by the broad plateau shown between 118 and

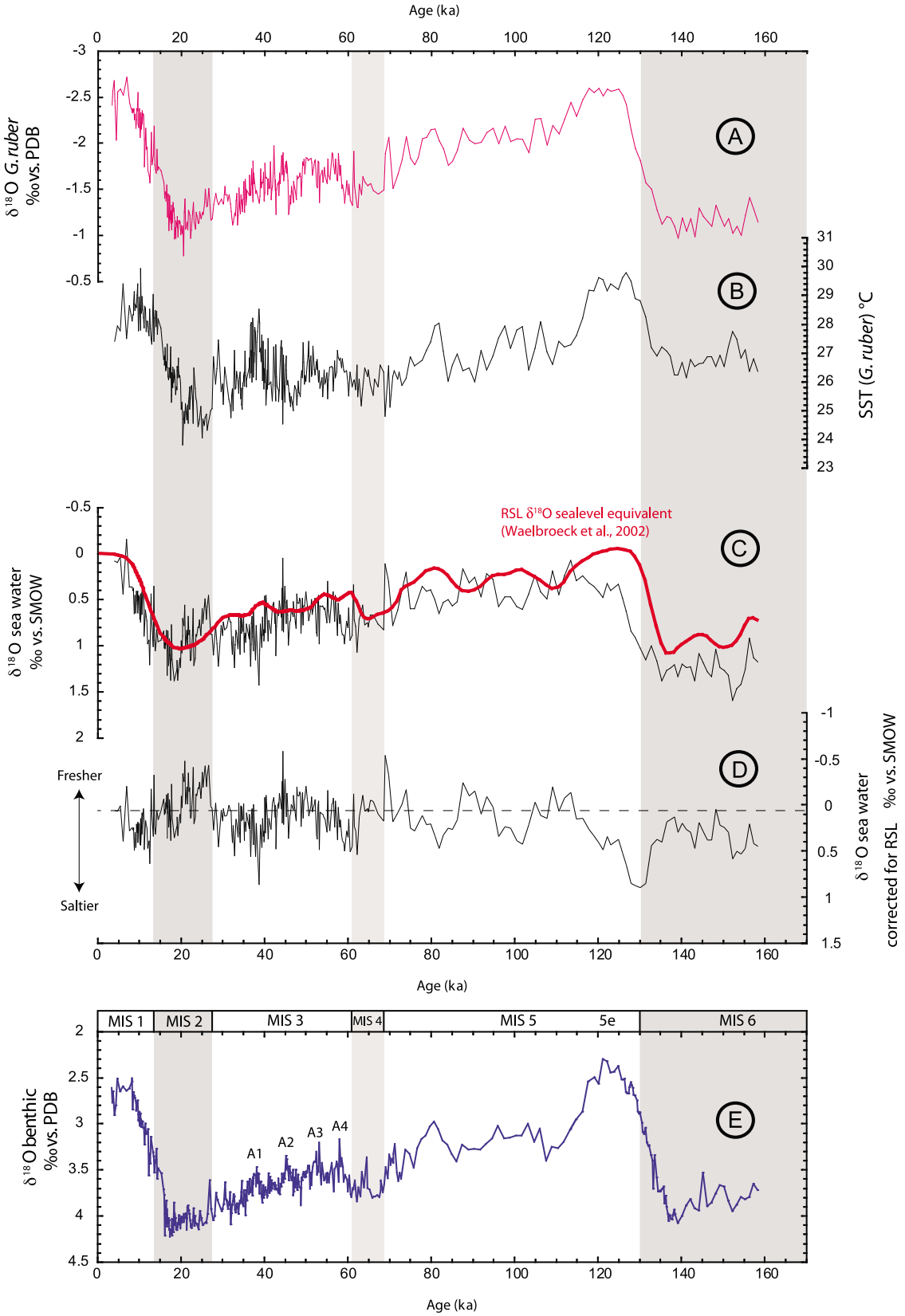
Age (ka)
δ18O G.ruber ‰vs.PDB
A
B
SST (G. ruber) °C
RSL δ18O sealevel equivalent (Waelbroeck et al., 2002)
C
δ18O sea water ‰ vs. SMOW
Fresher
Saltier
D
δ18O sea water corrected for RSL ‰ vs.SMOW
MIS 1
MIS 2
MIS 3
MIS 4
MIS 5
5e
MIS 6
δ18O benthic ‰vs.PDB
A1
A2
A3
A4
E

Figure 4

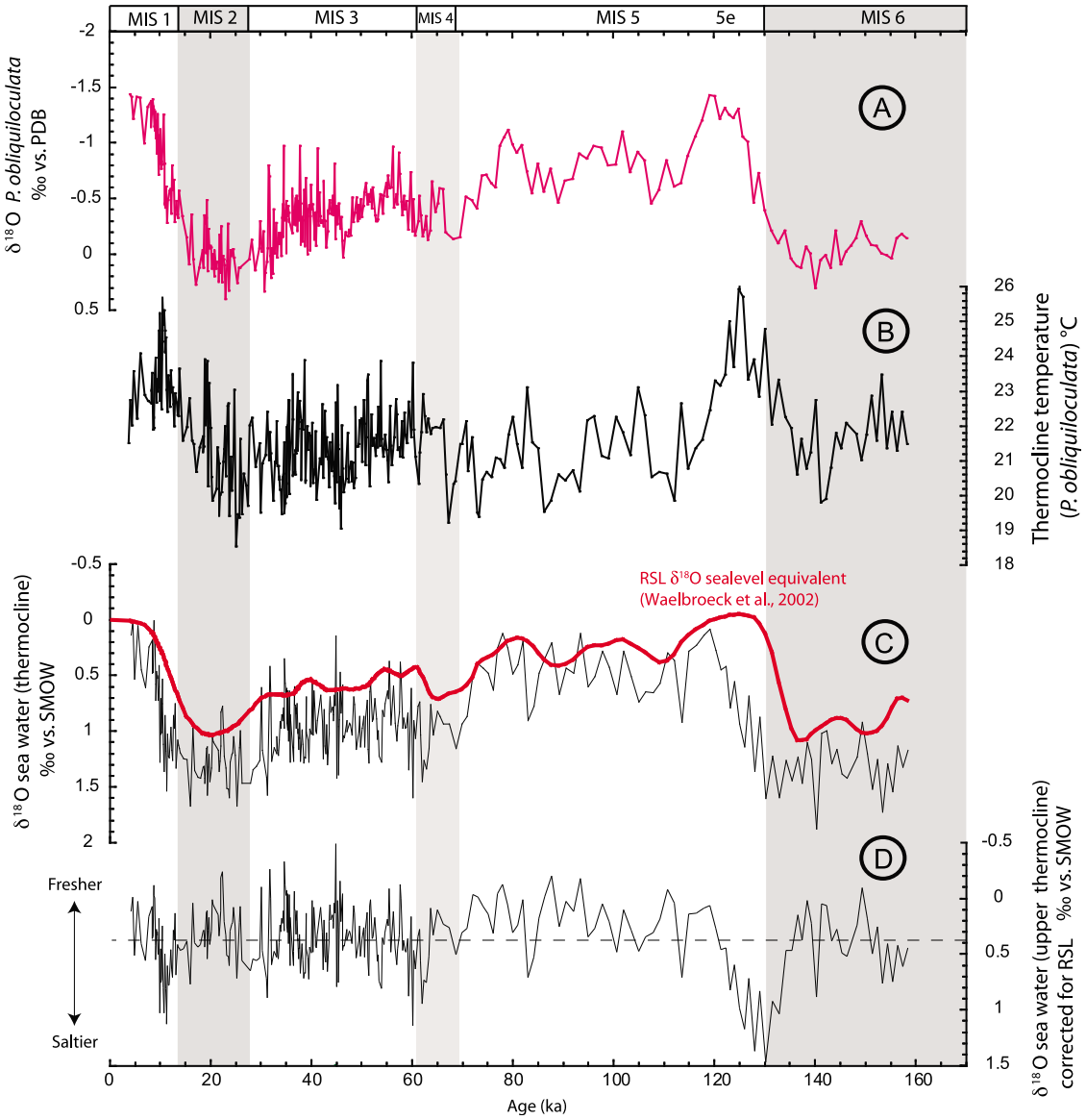

Figure 5. Upper thermocline hydrology over the last 160 kyr, based on analysis of *P. obliquiloculata* in Core MD06-3067. Note enhanced thermocline temperatures during MIS 5e and early Holocene. Shading marks glacial marine isotope stages (MIS 2, 4, and 6). (a) A $\delta^{18}O$ record of *P. obliquiloculata*. (b) Temperature of the upper themocline derived from Mg/Ca of *P. obliquiloculata*. (c) Thermocline $\delta^{18}O_{sw}$ uncorrected for sea level (thin black line). Solid red line indicates $\delta^{18}O$ sea level equivalent [from *Waelbroeck et al.*, 2002]. (d) Thermocline $\delta^{18}O_{sw}$ corrected for sea level. Dashed line indicates modern local $\delta^{18}O_{sw}$ of thermocline water.

Figure 4. Surface water hydrology over the last 160 kyr, based on analysis of *G. ruber* (white) in Core MD06-3067. Shading marks glacial marine isotope stages (MIS 2, 4, and 6). (a) A $\delta^{18}O$ record of *G. ruber* (white). (b) SST derived from Mg/Ca of *G. ruber* (white). Anomalously cold SST during MIS 3 and MIS 2 indicate phases of intensified upwelling. (c) Surface $\delta^{18}O_{sw}$ uncorrected for sea level (thin black line). Solid red line indicates $\delta^{18}O$ sea level equivalent [from *Waelbroeck et al.*, 2002]. (d) Surface $\delta^{18}O_{sw}$ corrected for sea level. Dashed line indicates modern local $\delta^{18}O_{sw}$ of surface water. (e) Benthic $\delta^{18}O$ record measured mainly on *P. wuellerstorfi* and *C. mundulus*.

127 ka in the *G. ruber* record. The transition from MIS 5e to 5d (118–108 ka) also differs significantly in the surface and thermocline signals: *G. ruber* shows a 2°C cooling, whereas *P. obliquiloculata* exhibits a decrease of 6°C, leading to cool thermocline temperatures during MIS 5d (20–21°C), which are only slightly warmer than during MIS 6 (21–22°C). Temperature fluctuations during MIS 5d–a are more marked in thermocline waters (23–20°C) than in surface waters (28–26°C). However, the MIS 5a to MIS 4 transition is better defined in the SST than in the thermocline record (28–25.5°C versus 23–21.5°C, respectively).

[31] During MIS 3, SST values exhibit high-amplitude variability (ranging from 28.5 to 24.5°C), showing prominent cooling episodes at ~49.5–46.5 ka and ~37–30 ka and warming pulses during stadials/Antarctic warm periods (notably during the Heinrich H4/A1 events). Thermocline temperatures fluctuate markedly (24–20°C) but show no distinct trend in contrast to SST, which clearly reflect stadials/Antarctic warm periods. Lowest SST (26–24°C) occurs during MIS 2 (27.5–19 ka), when SST displays a characteristic double trough. The glacial decrease in temperature is less distinct in the *P. obliquiloculata* thermocline record with values fluctuating between 20 and 23°C.

4.3.3. Surface and Thermocline $\delta^{18}O_{sw}$ (Sea Level Corrected)

[32] Sea level corrected surface $\delta^{18}O_{sw}$ show ~1‰ variability during the last glacial cycle (Figures 4c and 4d). This high-amplitude variability partly stems from the 1.5 kyr temporal resolution of the $\delta^{18}O$ sea level equivalent curve used for correction [*Waelbroeck et al.*, 2002], which is significantly lower than in our records (~200 years over the last glacial cycle). According to calibrations of $\delta^{18}O_{sw}$ in terms of salinity in the tropics (0.3‰/psu) [*LeGrande and Schmidt*, 2006; *Oppo et al.*, 2007], these variations correspond to a salinity change of up to ~3 psu, which is more than the present-day seasonal and regional variability [*Locarnini et al.*, 2006]. However, off Mindanao, changes in the $\delta^{18}O$ of precipitation and runoff potentially influenced the amplitude of $\delta^{18}O_{sw}$ fluctuations over the last glacial cycle. Transient increases in sea level corrected surface $\delta^{18}O_{sw}$ occur during MIS 3 stadials, whereas values decrease markedly at ~45 ka and during the LGM (26–19 ka), when SST were unusually cool. Reconstructed sea level corrected thermocline $\delta^{18}O_{sw}$ is generally slightly more enriched than today (~0.5‰), but does not show any significant glacial-interglacial trends (Figures 5c and 5d). The enrichment in surface and thermocline sea level corrected $\delta^{18}O_{sw}$ during Termination II apparently stems from age model inconsistencies between the sea level $\delta^{18}O$ equivalent [*Waelbroeck et al.*, 2002] used for correction and the MD06-3067 record.

4.4. Floral and Faunal Indicators of Paleoproductivity

[33] *Emiliana huxleyi* and *F. profunda* dominate the coccolith assemblage, representing more than 60% of the six major species recognized by the automated recognition system SYRACO (Figure 6a). A brief decrease of *F. profunda* to 45% during MIS 5 (at ~100 ka) coincides with an increase in the relative abundance of *G. ericsonii* from 15 to 30%. The two major species *F. profunda* and *E. huxleyi* show distinct long-term trends with *F. profunda* showing elevated abundances from MIS 6 to MIS 5c and in the Holocene, whereas *E. huxleyi* increases markedly in abundance from MIS 4 to the LGM. Since paleoproductivity is anticorrelated to the abundance of the deep dwelling species *F. profunda* [*Beaufort et al.*, 1997], it broadly correlates with the abundance of the shallow dwelling species *E. huxleyi* in Core MD06-3067. Highest productivity occurs during the LGM, MIS 3 and MIS 4 and lowest productivity during MIS 5e, whereas MIS 5d–5a and MIS 6 show intermediate values between these levels.

[34] Benthic foraminiferal abundances are closely related to the availability of food at the seafloor, which is largely derived from the export flux of primary production in the photic zone [*Loubere*, 1994, 1996]. In Core MD06-3067, there is considerable difference in the temporal distribution of the four major paleoproductivity indicators (Figures 6a–6d). Globobuliminids, which occur abundantly in tropical upwelling areas, show peaks in abundance (>8%) during MIS 2 and MIS 3 at ~18, 20, 24, 32–35, 45–50, 52 and 55 ka. During MIS 4 and MIS 6, globobuliminids vary between 3 and 8%, whereas abundances decrease to 0–2% during interglacials. Miliolids, typically reflecting mesotrophic conditions, exhibit a pronounced glacial-interglacial variability with abundances mostly >10% during MIS 2–4 and MIS 6 and dropping below 10% during interglacials. Globocassidulinids, which increase in numbers following seasonal phytodetritus pulses [*Gooday*, 1993], have their highest abundances during MIS 3 at ~37–41 ka (30 to >50%) and Termination II, whereas abundances generally remain between 10 and 30% in other intervals. *Bolivinita quadrilatera*, indicative of mesotrophic conditions, shows highest abundance during MIS 6 and the early part of Termination II (reaching >35%), then fluctuating below 15% from MIS 5e to the Holocene.

[35] In summary, both floral and faunal indicators exhibit distinct glacial-interglacial distribution patterns with lower productivity characterizing warm stages (MIS 5, Holocene) and increased productivity marking colder stages (MIS 6, MIS 4–2). Marked fluctuations in the composition of the coccolith and benthic foraminiferal assemblages suggest episodic increases during MIS 4–2, whereas productivity levels remained more stable and overall lower during MIS 6.

5. Discussion

5.1. Glacial-Interglacial SST Contrast

[36] SST estimates based on Mg/Ca of *G. ruber* in Core MD06-3067 reveal a sharp glacial-interglacial contrast offshore eastern Mindanao over the last 160 kyr (Figure 4b). SST shows an overall difference of ~3.5°C over Termination II and ~5°C over Termination I. In other areas of the WPWP, SST estimates exhibit consistent increases of ~3.5°C over Terminations I and II [*Lea et al.*, 2000, 2003; *Kienast et al.*, 2001; *Stott et al.*, 2002, 2007; *Visser et al.*, 2003; *Oppo and Sun*, 2005; *de Garidel-Thoron et al.*, 2007], except in the Sulu Sea, where lower values were estimated, based on foraminiferal counts and alkenones (2.2°C and 1°C, respectively) (T. de Garidel-Thoron et al., unpublished data, 2009). In Core MD06-3067, the higher SST contrast over Termination I is due to substantially cooler SST (by ~2°C) during

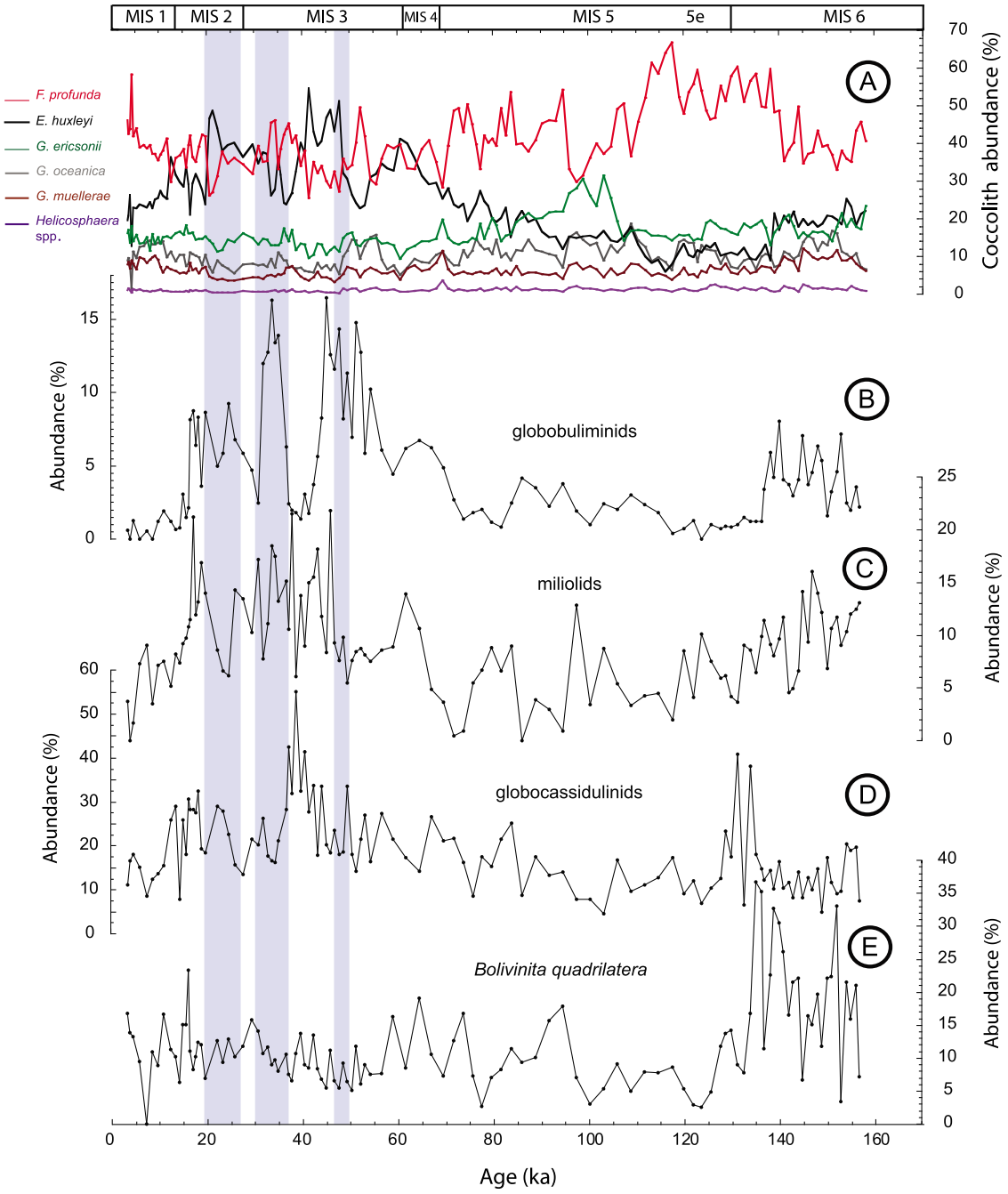

Figure 6. Relative percentage abundance of major coccolith and benthic foraminiferal high-productivity index taxa in Core MD06-3067. Blue bars indicate periods of intense surface and upper thermocline cooling, implying a reduced upper ocean temperature gradient. (a) Percent abundance of six major taxa within coccolith assemblages (*F. profunda*, *E. huxleyi*, *G. ericsonii*, *G. oceanica*, *G. muellerae*, and *Helicosphaera spp.*). (b) Percent abundance of globobuliminids. (c) Percent abundance of miliolids. (d) Percent abundance of globocassidulinids. (e) Percent abundance of *Bolivinita quadrilatera*.

the LGM than during MIS 6. These LGM values are colder (by ~1.5 to 2°C) than in other WPWP locations including the nearby Core MD98–2181 in the Davao Gulf, offshore southern Mindanao (Figure S1b in the auxiliary material) [*Stott et al.*, 2002].

[37] Further discrepancies in SST are evident during MIS 3, when we compare the records from the Davao Gulf (Core MD98–2181) [*Saikku et al.*, 2009] (Figure S1b) and offshore eastern Mindanao (Core MD06-3067). SST shows marked deviations (of 1–2°C) at ~55–53, 49.5–46.5, 39–36.5 and

33–31 ka, suggesting different controls on SST, related to local oceanographic settings. Site MD06-3067 represents a more open western Pacific location, strongly affected by upwelling of cool intermediate water masses, whereas Site MD98–2181 is located at the distal end of the Davao Gulf, which is separated by a shallow sill from the open Pacific Ocean (Figure 1). This sill extends over several hundred kilometers from South Mindanao to Miangas Island in water depths of just a few hundred meters (<800 m). We speculate that SST variability off eastern Mindanao during MIS 2 and MIS 3 is linked to changes in the intensity of the MC, which drives local upwelling. In contrast, SST variations in Core MD98-2181 appear related to millennial-scale atmospheric temperature variations in the Northern Hemisphere [*Saikku et al.*, 2009], and show close resemblance to SST patterns in the Sulu Sea [*Dannenmann et al.*, 2003] and South China Sea [*Kienast et al.*, 2001; *Oppo and Sun*, 2005].

5.2. Mindanao Dome Variability Over the Last 160 kyr

5.2.1. Long-Term Trends in Upper Ocean Thermal Structure

[38] Today, the Mindanao Dome affects the stratification of the upper water column along the eastern coast of Mindanao by influencing the depth of the thermocline (Figure 2). This deep upwelling system seasonally brings cold water up to 75 m water depth, thus causing the thermocline to dome up without having much effect on SST [*Udarbe-Walker and Villanoy*, 2001; *Tozuka et al.*, 2002]. The gradient between surface (*G. ruber*) and thermocline (*P. obliquiloculata*) temperatures in Core MD06-3067 provides a useful tool to reconstruct the degree of upward doming of the thermocline that is expressed in the thermal contrast within the upper water column over the last 160 kyr (Figure 7c). We infer that an increasing thermal gradient between surface and thermocline waters (ΔT°C) indicates stronger upward doming of isopcynals, hence a shoaling of the thermocline. However, upwelling of cooler waters to the surface results in a thicker mixed layer and depressed ΔT°C, thus we need also to monitor surface and thermocline temperatures to evaluate changes in upper ocean stratification.

[39] Two prominent episodes of thermocline warming occurred at ~11–9.5 ka and 130–126 ka, when thermocline temperatures reached 25–26°C, compared to average temperatures of 23–20°C (Figure 5b). The ΔT°C also decreased during these intervals, suggesting that dome activity was substantially reduced and cool upwelling waters did not reach the thermocline. In the later part of the Holocene and MIS 5e and over most of MIS 5, the ΔT°C increased to ~6–5°C, as thermocline temperature decreased, indicating renewed influence of the Mindanao Dome, at least comparable to the present day. In contrast to this view, *Kienast et al.* [2008] suggested a Holocene deepening of the nutricline/thermocline at the location of Core MD06-3067, based on nitrogen isotope evidence. In our records the Holocene decrease in productivity would support the latter interpretation, and thermocline cooling may reflect a general cooling of western Pacific intermediate water rather than advection of nutrient-rich cool deeper water.

[40] The MD06-3067 record reveals low thermocline temperatures (23–20°C) and a depressed ΔT°C during glacial periods, in particular during MIS 4–2, when sharp episodic declines in ΔT°C occur (down to ~3°C). We interpret these intervals as reflecting intense doming off Mindanao and vigorous upper ocean mixing. Enhanced activity of the Mindanao Dome during glacial times is supported by productivity proxies (coccoliths and benthic foraminifers; Figures 6a–6e), which indicate increased productivity during the LGM, most of MIS 3, MIS 4 and to a lesser extent during MIS 6. Globobuliminids, globocassidulinids and miliolids (Figures 6b and 6c), typical of elevated carbon flux at the seafloor, increase significantly during these intervals. High abundance of *B. quadrilatera* (Figure 6e) during MIS 6 is also diagnostic of enhanced export, but may reflect a different source of food, related to changes in local current systems.

[41] *Nakatsuka et al.* [1995] proposed that the dome became more active during glacials due to a strong East Asian winter monsoon. During glacial winters, enhanced high pressure over the Asian landmass plausibly intensified boreal winter monsoonal winds and strengthened the MC. In addition, the boreal winter monsoon season may have become prolonged by the southward shift of the ITCZ during glacial boreal summers. Terrestrial runoff proxy data from the same core indicate increased precipitation over Mindanao during MIS 2 and MIS 4 [*Kissel et al.*, 2010], which supports the contention of a southward shift in the boreal summer position of the ITCZ and/or intensification of the tropical convection [*Rosenthal et al.*, 2003; *Partin et al.*, 2007]. Dome activity appears to have been less intense during MIS 6 than during MIS 2, as shown by higher ΔT°C (~5–6°C) and productivity indicators. The intensity of the East Asian winter monsoon during MIS 6 remains controversial, as some studies suggest a strong monsoon regime [*Xiao et al.*, 1999; *Chen et al.*, 2000], whereas others indicate weakening of the monsoon [*Guo et al.*, 2009; *Rousseau et al.*, 2009]. Our results support a weaker winter monsoon during MIS 6 than during MIS 2, although considerably enhanced in comparison to interglacials.

5.2.2. Millennial-Scale Variability During MIS 3 and MIS 2

[42] Superimposed on the long-term trends are a number of significant millennial-scale variations during MIS 4–2. Several transient intervals of highest productivity (carbon flux to the seafloor), marked by peak abundance in *Globobulimin*a spp. (>8%; Figure 6b), are evident between 17 and 55 ka. Most of these intervals are characterized by unusually sharp drops in SST (down to ~24–26°C at ~49.5–46.5, 37–30 and 27.5–19 ka; Figure 7a) and by a depressed upper ocean thermal gradient (below 4°C within the upper ~100 m; Figure 7c). Today, *Globobulimina* spp. represent the most common species in major upwelling areas such as the Arabian Sea and eastern Pacific [*Jannink et al.*, 1998; *Cannariato et al.*, 1999]. The coincidence between high primary productivity and unusually low SST at this WPWP location suggests nutrient enrichment through upwelling of cooler middepth waters to the ocean surface. Enriched nutrient supply to the mixed layer is supported by elevated abundance of *E. huxleyi* (shallow photic zone producer) in the coccolith assemblages (Figure 6a). Additional evidence of surface upwelling is provided by AMS^{14}C dates derived from surface dwelling planktic foraminifers. AMS^{14}C dates in two

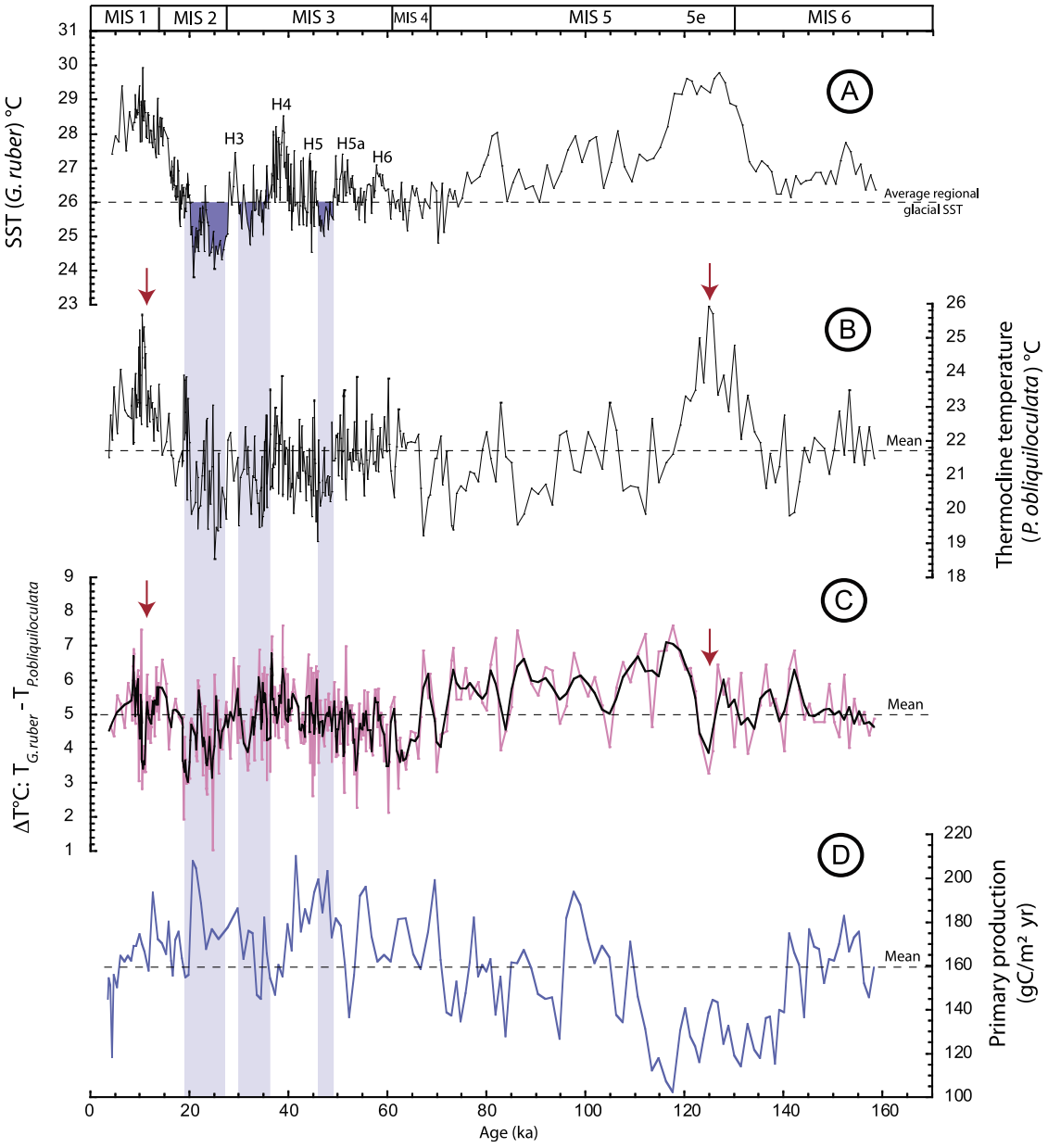

Figure 7. Records of surface-to-thermocline temperature contrast and primary productivity from Core MD06-3067. Blue bars indicate periods of intense surface and upper thermocline cooling, implying a reduced upper ocean temperature gradient. Red arrows mark prominent collapses of Mindanao Dome during MIS 5e and early Holocene. (a) *G. ruber* (white) Mg/Ca–derived SST. Dashed line indicates average regional glacial SST. (b) *P. obliquiloculata* Mg/Ca–derived thermocline water temperature. Dashed line indicates mean thermocline temperature over the last 160 kyr. (c) Thermal gradient between surface and thermocline waters ($\Delta T°C = T_{surface} - T_{thermocline}$). The profile was computed as the difference between SST and thermocline temperature shown in Figures 4b and 5b. Dashed line indicates mean thermal gradient over the last 160 kyr. (d) Primary production estimated from relative abundance of the coccolith species *F. profunda*. Dashed line indicates mean primary production over the last 160 kyr.

glacial samples (KIA 35211 and KIA 35212) indicate ages ~1800 and ~3000 years older than ages based on our age model (19.6 and 22.1 ka versus 17.8 and 19.1 ka, respectively). These age offsets can be explained by upwelling of older, deeper water to the surface during periods of intensified dome activity.

[43] The SST record also provides evidence of sea surface warming during Heinrich events H3, H4, H5, H5a and H6

(Figure 7). This is in sharp contrast to most other records from the WPWP, which exhibit a northern hemisphere signal, characterized by surface cooling during stadials (Heinrich events) and warming during interstadials [*Kienast et al.*, 2001; *Dannenmann et al.*, 2003; *Oppo and Sun*, 2005; *Saikku et al.*, 2009]. Whereas these WPWP records appear to be mainly influenced by atmospheric teleconnections, episodes of sea surface warming at the location of Core MD06-3067 likely reflect periodic decreases in the intensity of the MC and concomitant decreases in upwelling and upper ocean mixing during Heinrich events. We suggest that millennial-scale variations in the Mindanao Dome upwelling during MIS 3 were linked to oscillations in the maximum displacement of the ITCZ and attendant changes in monsoonal wind and surface current circulation systems in response to high-latitude climate forcing.

5.3. Significance of Mindanao Dome for Regional Climate and Ocean Dynamics

[44] The Mindanao Dome is situated at a major tropical water mass crossroad, and it interacts with a number of climatic features, notably the East Asian winter monsoon, the meridional and zonal heat transfer linked to NEC variability and ENSO state and the interocean heat, salt and nutrient transfer via the ITF. In their investigation of the Mindanao Dome's seasonal dynamics, *Masumoto and Yamagata* [1991] suggested that local upwelling intensified during the East Asian winter monsoon, when a positive wind stress curl (cyclonic circulation) increases in the region. Since the Mindanao dome is forced by strong northeasterly, coast parallel winds, the intensity of the dome is directly related to the strength of the East Asian winter monsoon.

[45] ENSO influences the structure and intensity of the Mindanao Dome upwelling due to the strong coupling between the northeasterly wind regime (East Asian winter monsoon) and the El Niño phenomenon. Today, the mature phase of El Niño often occurs during boreal winter, and is usually accompanied by a weaker winter monsoon along the East Asian coast resulting in warmer and wetter winter conditions over SE Asia [*Wang et al.*, 2000]. Thus, the variability of the Mindanao Dome provides a direct indicator of the ENSO state, as upwelling intensifies when a strong cyclonic gyre becomes established during La Niña conditions, whereas strong El Niño events tend to suppress the cyclonic circulation, reducing Ekman transport.

[46] During MIS 2, vigorous upwelling provides evidence of a strongly enhanced East Asian winter monsoon and prevailing La Niña conditions. Increased upper ocean mixing in the Sulu Sea [*de Garidel-Thoron et al.*, 2001] and the South China Sea [*Steinke et al.*, 2010] additionally supports strengthening of the East Asian winter monsoon during MIS 2. In contrast, local warming during stadials indicates reduced upwelling and prevalence of El Niño–like conditions during episodes of weaker meridional overturning circulation. These findings are in agreement with high-resolution $\delta^{18}O_{seawater}$ records from the Davao Bay [*Stott et al.*, 2002; *Saikku et al.*, 2009] and the Sulu Sea [*Dannenmann et al.*, 2003] and cave $\delta^{18}O$ records from Borneo [*Partin et al.*, 2007], which were interpreted as reflecting more frequent El Niño events during stadials.

[47] Changes in the intensity of the MC, which drives upwelling, have major repercussions in both the zonal and meridional redistribution of heat in the equatorial Pacific. The Mindanao Dome is situated within the ITF main inflow area from the Pacific, thus influencing the heat, salt and nutrient budget of ITF waters. Today, inflowing waters are characterized by a distinct salinity maximum within the upper thermocline. Intense vertical mixing along the ITF pathway as well as freshwater export from the Java Sea radically alter the stratification of the upper water column, resulting in an unusually fresh and cool subsurface outflow with a steep thermocline and no distinct salinity stratification [*Gordon*, 2005]. Opening of the freshwater portal through the Java Sea in the early Holocene (~9.5 ka) led to intensification of the ITF thermocline flow and reduction of the surface component downstream of the Makassar Strait [*Xu et al.*, 2010]. Therefore, since the early Holocene, the freshwater export from the South China Sea has exerted a more important control on the heat and salt export into the Indian Ocean than the primary composition of Pacific inflow waters.

[48] However, during the LGM, the ITF acted as a more direct conduit of Pacific surface and thermocline waters because the South China Sea was disconnected from the ITF. Increased upwelling of the Mindanao Dome promoted inflow of cooler, nutrient-enriched waters with reduced vertical stratification, and vigorous mixing within the narrower glacial passages further decreased stratification of ITF outflow waters [*Xu et al.*, 2010]. Evidence for a glacial nutrient-enriched ITF is preserved in Eastern Indian Ocean productivity records such as the silicon-rich upwelling of ITF water masses at Ninetyeast Ridge [*Broecker et al.*, 2000]. Glacial productivity maxima were also reported from the ITF outflow within the Timor Sea [*Müller and Opdyke*, 2000; *Holbourn et al.*, 2005; *Kawamura et al.*, 2006], suggesting that the ITF provided a major channel for nutrient export from the Pacific to Indian Oceans, although it remains unclear to what extent nutrient enrichment within the Indonesian seas by mixing or runoff enhanced productivity in the eastern Indian Ocean.

[49] The northwestern edge of the Mindanao dome is also the place where the NEC bifurcates into the MC and Kuroshio Current, which form the main pathways for meridional heat transfer in the Pacific and exert major control on SE Asian and NW Pacific climate. SST records from the Okinawa Trough indicate weakening of the Kuroshio during Heinrich events, hence reduced heat transfer toward the high latitudes [*Li et al.*, 2001; *Xiang et al.*, 2007]. On short time scales, there is evidence that the variability of the Kuroshio and Mindanao currents is linked to the ITCZ seasonal migration [*Qu et al.*, 2008] and ENSO state [*Yamagata et al.*, 1985], which strongly influence monsoonal winds. On longer time scales, the position and intensity of these currents appear to be mainly determined by changes in the interhemispheric temperature gradient, exposure or flooding of extensive tropical shelves related to sea level and prevalent radiative forcing. Taking these features and considerations together, the Mindanao Dome is an oceanographic feature within the WPWP with implications to the climatology of the wider region and beyond. This makes the dome a feature of particular interest, when attempting to unravel changes in western Pacific

atmospheric and oceanographic circulation patterns and how they may be linked to far-field climatic influences from the high latitudes.

6. Conclusion

[50] Paleoproductivity indicators, SST and thermocline temperature reconstructions in Core MD06-3067 reveal considerable glacial-interglacial as well as suborbital variability in the activity of the Mindanao Dome over the last 160 kyr. Evidence for periodic glacial upwelling during MIS 2 and MIS 3 is provided by enhanced surface productivity, unusually low SST, low thermal gradient within the upper water column and remarkably old AMS^{14}C ages of surface dwelling foraminifers that indicate a surface layer radiocarbon reservoir age between ~1800 and ~3000 years. Sea surface warming during Heinrich events mark periodic collapses of the Mindanao Dome upwelling during MIS 3. We attribute the successive surface warmings and coolings during MIS 2 and MIS 3 to changes in the ENSO state and associated latitudinal shifts in the ITCZ position that affected boreal winter monsoonal winds and upper ocean circulation patterns. Our results indicate that La Niña conditions prevailed during the LGM, whereas an El Niño–like mode dominated during Heinrich events. Dome activity differed substantially over the last two glacial cycles: intense Ekman transport led to episodic upwelling during MIS 2 and MIS 3, whereas the upper ocean remained more stratified during MIS 6. Since monsoonal winds strongly influence the intensity of the Mindanao Current [*Masumoto and Yamagata*, 1991] driving regional upwelling off eastern Mindanao, our records provide a proxy for the intensity of the East Asian winter monsoon.

[51] **Acknowledgments.** We thank Yvon Balut, the crew of R/V *Marion Dufresne*, and the French Polar Institute (IPEV) for all their efforts and support during the Marco Polo 2 Cruise (IMAGES program). We are grateful to Marcus Regenberg and Guillaume Leduc for helpful discussions, to Jian Xu for advice regarding Mg/Ca analysis, and to Brigitte Salomon and Karin Kissling for technical assistance. We also thank the editor, Rainer Zahn; Helen Neil; and one anonymous reviewer for insightful, constructive comments. This research was funded in Germany by the Deutsche Forschungsgemeinschaft (DFG grant Ku649/26-1), in France by the Commissariat à l'Energie Atomique (CEA) and the Centre National de la Recherche Scientifique (CNRS), and in Canada by the Natural Sciences and Engineering Research Council of Canada (NSERC) and the Canadian Institute for Advanced Research (CIFAR).

References

Anand, P., H. Elderfield, and M. H. Conte (2003), Calibration of Mg/Ca thermometry in planktonic foraminifera from a sediment trap time series, *Paleoceanography*, *18*(2), 1050, doi:10.1029/2002PA000846.

Antonov, J. I., R. A. Locarnini, T. P. Boyer, A. V. Mishonov, and H. E. Garcia (2006), *World Ocean Atlas 2005*, vol. 2, *Salinity*, *NOAA Atlas NESDIS*, vol. 62, edited by S. Levitus, 182 pp., NOAA, Silver Spring, Md.

Beaufort, L., and D. Dollfus (2004), Automatic recognition of coccoliths by dynamical neural networks, *Mar. Micropaleontol.*, *51*(1–2), 57–73, doi:10.1016/j.marmicro.2003.09.003.

Beaufort, L., Y. Lancelot, P. Camberlin, O. Cayre, E. Vincent, F. Bassinot, and L. Labeyrie (1997), Insolation cycles as a major control equatorial Indian Ocean primary production, *Science*, *278*, 1451–1454, doi:10.1126/science.278.5342.1451.

Beaufort, L., T. de Garidel-Thoron, A. C. Mix, and N. G. Pisias (2001), ENSO-like forcing on oceanic primary production during the Late Pleistocene, *Science*, *293*, 2440–2444, doi:10.1126/science.293.5539.2440.

Bemis, B. E., H. J. Spero, J. Bijma, and D. W. Lea (1998), Reevaluation of the oxygen isotopic composition of planktonic foraminifera: Experimental results and revised paleotemperature equations, *Paleoceanography*, *13*(2), 150–160, doi:10.1029/98PA00070.

Bian, N., and P. A. Martin (2010), Investigating the fidelity of Mg/Ca and other elemental data from reductively cleaned planktonic foraminifera, *Paleoceanography*, *25*, PA2215, doi:10.1029/2009PA001796.

Broecker, W. S., E. Clark, J. Lynch-Stieglitz, W. Beck, L. D. Stott, I. Hajdas, and G. Bonani (2000), Late glacial diatom accumulation at 9°S in the Indian Ocean, *Paleoceanography*, *15*(3), 348–352, doi:10.1029/1999PA000439.

Cannariato, K. G., J. P. Kennett, and R. J. Behl (1999), Biotic response to late Quaternary rapid climate switches in Santa Barbara Basin: Ecological and evolutionary implications, *Geology*, *27*(1), 63–66, doi:10.1130/0091-7613(1999)027<0063:BRTLQR>2.3.CO;2.

Chen, F. H., Z. D. Feng, and J. W. Zhang (2000), Loess particle size data indicative of stable winter monsoons during the last interglacial in the western part of the Chinese Loess Plateau, *Catena*, *39*(4), 233–244, doi:10.1016/S0341-8162(00)00083-7.

Cléroux, C., E. Cortijo, J.-C. Duplessy, and R. Zahn (2007), Deep-dwelling foraminifera as thermocline temperature recorders, *Geochem. Geophys. Geosyst.*, *8*, Q04N11, doi:10.1029/2006GC001474.

Dannenmann, S., B. K. Linsley, D. W. Oppo, Y. Rosenthal, and L. Beaufort (2003), East Asian monsoon forcing of suborbital variability in the Sulu Sea during Marine Isotope Stage 3: Link to Northern Hemisphere climate, *Geochem. Geophys. Geosyst.*, *4*(1), 1001, doi:10.1029/2002GC000390.

de Garidel-Thoron, T., L. Beaufort, B. K. Linsley, and S. Dannenmann (2001), Millennial-scale dynamics of the east Asian winter monsoon during the last 200,000 years, *Paleoceanography*, *16*(5), 491–502, doi:10.1029/2000PA000557.

de Garidel-Thoron, T., Y. Rosenthal, L. Beaufort, E. Bard, C. Sonzogni, and A. C. Mix (2007), A multiproxy assessment of the western equatorial Pacific hydrography during the last 30 kyr, *Paleoceanography*, *22*, PA3204, doi:10.1029/2006PA001269.

de Villiers, S., M. Greaves, and H. Elderfield (2002), An intensity ratio calibration method for the accurate determination of Mg/Ca and Sr/Ca of marine carbonates by ICP-AES, *Geochem. Geophys. Geosyst.*, *3*(1), 1001, doi:10.1029/2001GC000169.

Dekens, P. S., D. W. Lea, D. K. Pak, and H. J. Spero (2002), Core top calibration of Mg/Ca in tropical foraminifera: Refining paleotemperature estimation, *Geochem. Geophys. Geosyst.*, *3*(4), 1022, doi:10.1029/2001GC000200.

Dollfus, D., and L. Beaufort (1999), Fat neural network for recognition of position-normalised objects, *Neural Netw.*, *12*(3), 553–560, doi:10.1016/S0893-6080(99)00011-8.

Fairbanks, R. G., M. N. Evans, J. L. Rubenstone, K. Broad, M. D. Moore, and C. D. Charles (1997), Evaluating climate indices and their geochemical proxies measured in corals, *Coral Reefs*, *16*, S93–S100, doi:10.1007/s003380050245.

Fairbanks, R. G., R. A. Mortlock, T. C. Chiu, L. Cao, A. Kaplan, T. P. Guilderson, T. W. Fairbanks, A. L. Bloom, P. M. Grootes, and M. J. Nadeau (2005), Radiocarbon calibration curve spanning 0 to 50,000 years BP based on paired Th-230/U-234/U-238 and C-14 dates on pristine corals, *Quat. Sci. Rev.*, *24*(16–17), 1781–1796, doi:10.1016/j.quascirev.2005.04.007.

Farmer, E. C., A. Kaplan, P. B. de Menocal, and J. Lynch-Stieglitz (2007), Corroborating ecological depth preferences of planktonic foraminifera in the tropical Atlantic with the stable oxygen isotope ratios of core top specimens, *Paleoceanography*, *22*, PA3205, doi:10.1029/2006PA001361.

Fine, R., R. Lukas, F. Bingham, M. Warner, and R. Gammon (1994), The western equatorial Pacific: A water mass crossroads, *J. Geophys. Res.*, *99*(C12), 25,063–25,080, doi:10.1029/94JC02277.

Firing, E., Y. Kashino, and P. Hacker (2005), Energetic subthermocline currents observed east of Mindanao, *Deep Sea Res., Part II*, *52*(3–4), 605–613, doi:10.1016/j.dsr2.2004.12.007.

Gooday, A. J. (1993), Deep-sea benthic foraminiferal species which exploit phytodetritus: Characteristic features and controls on distribution, *Mar. Micropaleontol.*, *22*, 187–205, doi:10.1016/0377-8398(93)90043-W.

Gordon, A. L. (2005), The Indonesian Seas: Oceanography of the Indonesian Seas and their throughflow, *Oceanography*, *18*(4), 14–27.

Gordon, A. L., and J. L. McClean (1999), Thermohaline stratification of the Indonesian Seas: Model and observations, *J. Phys. Oceanogr.*,

29(2), 198–216, doi:10.1175/1520-0485(1999)029<0198:TSOTIS>2.0.CO;2.

Greaves, M., et al. (2008), Interlaboratory comparison study of calibration standards for foraminiferal Mg/Ca thermometry, *Geochem. Geophys. Geosyst.*, *9*, Q08010, doi:10.1029/2008GC001974.

Guillou, H., B. S. Singer, C. Laj, C. Kissel, S. Scaillet, and B. R. Jicha (2004), On the age of the Laschamp geomagnetic excursion, *Earth Planet. Sci. Lett.*, *227*(3–4), 331–343, doi:10.1016/j.epsl.2004.09.018.

Guo, Z. T., A. Berger, Q. Z. Yin, and L. Qin (2009), Strong asymmetry of hemispheric climates during MIS-13 inferred from correlating China loess and Antarctica ice records, *Clim. Past*, *5*(1), 21–31, doi:10.5194/cp-5-21-2009.

Hemleben, C., M. Spindler, and O. R. Anderson (1989), *Modern Planktonic Foraminifera*, Springer, New York.

Holbourn, A., W. Kuhnt, H. Kawamura, Z. Jian, P. Grootes, H. Erlenkeuser, and J. Xu (2005), Orbitally paced paleoproductivity variations in the Timor Sea and Indonesian Throughflow variability during the last 460 kyr, *Paleoceanography*, *20*, PA3002, doi:10.1029/2004PA001094.

Jannink, N. T., W. J. Zachariasse, and G. J. Van der Zwaan (1998), Living (Rose Bengal stained) benthic foraminifera from the Pakistan continental margin (northern Arabian Sea), *Deep Sea Res., Part I*, *45*(9), 1483–1513, doi:10.1016/S0967-0637(98)00027-2.

Kalnay, E., et al. (1996), The NCEP/NCAR 40-Year Reanalysis Project, *Bull. Am. Meteorol. Soc.*, *77*(3), 437–471, doi:10.1175/1520-0477(1996)077<0437:TNYRP>2.0.CO;2.

Kawamura, H., A. Holbourn, and W. Kuhnt (2006), Climate variability and land–ocean interactions in the Indo Pacific Warm Pool: A 460-ka palynological and organic geochemical Record from the Timor Sea, *Mar. Micropaleontol.*, *59*, 1–14, doi:10.1016/j.marmicro.2005.09.001.

Kienast, M., S. Steinke, K. Stattegger, and S. E. Calvert (2001), Synchronous tropical South China Sea SST change and Greenland warming during deglaciation, *Science*, *291*, 2132–2134, doi:10.1126/science.1057131.

Kienast, M., M. F. Lehmann, A. Timmermann, E. Galbraith, T. Bolliet, A. Holbourn, C. Normandeau, and C. Laj (2008), A mid-Holocene transition in the nitrogen dynamics of the western equatorial Pacific: Evidence of a deepening thermocline?, *Geophys. Res. Lett.*, *35*, L23610, doi:10.1029/2008GL035464.

Kissel, C., C. Laj, M. Kienast, T. Bolliet, A. Holbourn, P. Hill, W. Kuhnt, and P. Braconnot (2010), Monsoon variability and deep oceanic circulation in the western equatorial Pacific over the last climatic cycle: Insights from sedimentary magnetic properties and sortable silt, *Paleoceanography*, *25*, PA3215, doi:10.1029/2010PA001980.

Kuhnt, W., S. Hess, and Z. M. Jian (1999), Quantitative composition of benthic foraminiferal assemblages as a proxy indicator for organic carbon flux rates in the South China Sea, *Mar. Geol.*, *156*(1–4), 123–157, doi:10.1016/S0025-3227(98)00176-5.

Laj, C., et al. (2006), Les rapports de campagnes à la mer: MD155-Marco Polo 2, IMAGES XIV cruise report, 11 juin au 6 juillet 2006, *Publ. Inst. Polaire Fr. OCE/2006/06*, Publ. de Inst. Polaire Fr., Brest, France.

Lea, D. W., D. K. Pak, and H. J. Spero (2000), Climate impact of late quaternary equatorial Pacific sea surface temperature variations, *Science*, *289*, 1719–1724, doi:10.1126/science.289.5485.1719.

Lea, D. W., D. K. Pak, L. C. Peterson, and K. A. Hughen (2003), Synchroneity of tropical and high-latitude Atlantic temperatures over the last glacial termination, *Science*, *301*, 1361–1364, doi:10.1126/science.1088470.

LeGrande, A. N., and G. A. Schmidt (2006), Global gridded data set of the oxygen isotopic composition in seawater, *Geophys. Res. Lett.*, *33*, L12604, doi:10.1029/2006GL026011.

Li, T., Z. Liu, M. A. Hall, S. Berne, Y. Saito, S. Cang, and Z. Cheng (2001), Heinrich event imprints in the Okinawa Trough: Evidence from oxygen isotope and planktonic foraminifera, *Palaeogeogr. Palaeoclimatol. Palaeoecol.*, *176*, 133–146, doi:10.1016/S0031-0182(01)00332-7.

Lin, H. L., and H. Y. Hsieh (2007), Seasonal variations of modern planktonic foraminifera in the South China Sea, *Deep Sea Res., Part II*, *54*, 1634–1644, doi:10.1016/j.dsr2.2007.05.007.

Lin, H. L., W. C. Wang, and G. W. Hung (2004), Seasonal variation of planktonic foraminiferal isotopic composition from sediment traps in the South China Sea, *Mar. Micropaleontol.*, *53*, 447–460, doi:10.1016/j.marmicro.2004.08.004.

Locarnini, R. A., A. V. Mishonov, J. I. Antonov, T. P. Boyer, and H. E. Garcia (2006), *World Ocean Atlas 2005*, vol. 1, *Temperature*, *NOAA Atlas NESDIS*, vol. 61, edited by S. Levitus, 182 pp., NOAA, Silver Spring, Md.

Loubere, P. (1994), Quantitative estimation of surface ocean productivity and bottom water oxygen concentration using benthic foraminifera, *Paleoceanography*, *9*, 723–737, doi:10.1029/94PA01624.

Loubere, P. (1996), The surface ocean productivity and bottom water oxygen signals in deep water benthic foraminiferal assemblages, *Mar. Micropaleontol.*, *28*, 247–261, doi:10.1016/0377-8398(96)00004-7.

Lukas, R. (1988), Interannual fluctuations of the Mindanao Current Inferred from sea level, *J. Geophys. Res.*, *93*(C6), 6744–6748, doi:10.1029/JC093iC06p06744.

Lukas, R., E. Firing, P. Hacker, P. L. Richardson, C. A. Collins, R. Fine, and R. Gammon (1991), Observations of the Mindanao Current during the Western Equatorial Pacific-Ocean Circulation Study, *J. Geophys. Res.*, *96*(C4), 7089–7104, doi:10.1029/91JC00062.

Lyon, B., H. Cristi, E. R. Verceles, F. D. Hilario, and R. Abastillas (2006), Seasonal reversal of the ENSO rainfall signal in the Philippines, *Geophys. Res. Lett.*, *33*, L24710, doi:10.1029/2006GL028182.

Martin, P. A., and D. W. Lea (2002), A simple evaluation of cleaning procedures on fossil benthic foraminiferal Mg/Ca, *Geochem. Geophys. Geosyst.*, *3*(10), 8401, doi:10.1029/2001GC000280.

Masumoto, Y., and T. Yamagata (1991), Response of the Western Tropical Pacific to the Asian Winter Monsoon: The Generation of the Mindanao Dome, *J. Phys. Oceanogr.*, *21*(9), 1386–1398, doi:10.1175/1520-0485(1991)021<1386:ROTWTP>2.0.CO;2.

Masuzawa, J. (1968), Second cruise for CSK, Ryofu Maru, January to March 1968, *Oceanogr. Mag.*, *20*, 173–185.

Mohtadi, M., S. Steinke, J. Groeneveld, H. G. Fink, T. Rixen, D. Hebbeln, B. Donner, and B. Herunadi (2009), Low-latitude control on seasonal and inter-annual changes in planktonic foraminiferal flux and shell geochemistry off south Java: A sediment trap study, *Paleoceanography*, *24*, PA1201, doi:10.1029/2008PA001636.

Müller, A., and B. N. Opdyke (2000), Glacial-interglacial changes in nutrient utilization and paleoproductivity in the Indonesian Throughflow sensitive Timor Trough, easternmost Indian Ocean, *Paleoceanography*, *15*(1), 85–94, doi:10.1029/1999PA900046.

Nadeau, M. J., M. Schleicher, P. M. Grootes, H. Erlenkeuser, A. Gottdang, D. J. W. Mous, J. M. Sarnthein, and H. Willkomm (1997), The Leibniz-Labor AMS facility at the Christian-Albrechts Univ., Kiel, Germany, *Nucl. Instrum. Methods Phys. Res., Sect. B*, *123*(1–4), 22–30, doi:10.1016/S0168-583X(96)00730-6.

Nakatsuka, T., N. Harada, E. Matsumoto, N. Handa, T. Oba, M. Ikehara, H. Matsuoka, and K. Kimoto (1995), Glacial-interglacial migration of an upwelling field in the Western Equatorial Pacific recorded by sediment $^{15}N/^{14}N$, *Geophys. Res. Lett.*, *22*, 2525–2528, doi:10.1029/95GL02544.

Oppo, D. W., and Y. B. Sun (2005), Amplitude and timing of sea-surface temperature change in the northern South China Sea: Dynamic link to the East Asian monsoon, *Geology*, *33*(10), 785–788, doi:10.1130/G21867.1.

Oppo, D. W., B. K. Linsley, Y. Rosenthal, S. Dannenmann, and L. Beaufort (2003), Orbital and suborbital climate variability in the Sulu Sea, western tropical Pacific, *Geochem. Geophys. Geosyst.*, *4*(1), 1003, doi:10.1029/2001GC000260.

Oppo, D. W., G. A. Schmidt, and A. N. LeGrande (2007), Seawater isotope constraints on tropical hydrology during the Holocene, *Geophys. Res. Lett.*, *34*, L13701, doi:10.1029/2007GL030017.

Partin, J. W., K. M. Cobb, J. F. Adkins, B. Clark, and D. P. Fernandez (2007), Millennial-scale trends in West Pacific Warm Pool hydrology since the Last Glacial Maximum, *Nature*, *449*, 452–455, doi:10.1038/nature06164.

Qu, T. D., H. Mitsudera, and T. Yamagata (1999), A climatology of the circulation and water mass distribution near the Philippine coast, *J. Phys. Oceanogr.*, *29*(7), 1488–1505, doi:10.1175/1520-0485(1999)029<1488:ACOTCA>2.0.CO;2.

Qu, T., J. Gan, A. Ishida, Y. Kashino, and T. Tozuka (2008), Semiannual variation in the western tropical Pacific Ocean, *Geophys. Res. Lett.*, *35*, L16602, doi:10.1029/2008GL035058.

Ravelo, A. C., and R. G. Fairbanks (1992), Oxygen isotopic composition of multiple species of planktonic foraminifera: Recorders of the modern photic zone temperature gradient, *Paleoceanography*, *7*, 815–832, doi:10.1029/92PA02092.

Rosenthal, Y., D. W. Oppo, and B. K. Linsley (2003), The amplitude and phasing of climate change during the last deglaciation in the Sulu Sea, western equatorial Pacific, *Geophys. Res. Lett.*, *30*(8), 1428, doi:10.1029/2002GL016612.

Rosenthal, Y., et al. (2004), Interlaboratory comparison study of Mg/Ca and Sr/Ca measurements in planktonic foraminifera for paleoceanographic research, *Geochem. Geophys. Geosyst.*, *5*, Q04D09, doi:10.1029/2003GC000650.

Rousseau, D. D., N. Wu, Y. Pei, and F. Li (2009), Three exceptionally strong East-Asian summer monsoon events during glacial times in the past 470 kyr, *Clim. Past*, *5*, 157–169, doi:10.5194/cp-5-157-2009.

Rudolf, B., A. Becker, U. Schneider, A. Meyer-Christoffer, and M. Ziese (2010), On the most

recent gridded global data set issued in fall 2010 by the Global Precipitation Climatology Center (GPCC), GPCC Status Report, 7 pp.

Ruth, U., et al. (2007), "EDML1": A chronology for the EPICA deep ice core from Dronning Maud Land, Antarctica, over the last 150 000 years, *Clim. Past*, *3*, 475–484, doi:10.5194/cp-3-475-2007.

Saikku, R., L. Stott, and R. Thunell (2009), A bi-polar signal recorded in the western tropical Pacific: Northern and Southern Hemisphere climate records from the Pacific warm pool during the last Ice Age, *Quat. Sci. Rev.*, *28*(23–24), 2374–2385, doi:10.1016/j.quascirev.2009.05.007.

Sakai, K., and R. Kawamura (2009), Remote response of the East Asian winter monsoon to tropical forcing related to El Niño–Southern Oscillation, *J. Geophys. Res.*, *114*, D06105, doi:10.1029/2008JD010824.

Schleicher, M., P. M. Grootes, M. J. Nadeau, and A. Schoon (1998), The carbonate C-14 background and its components at the Leibniz AMS facility, *Radiocarbon*, *40*(1), 85–93.

Schmidt, M. W., H. J. Spero, and D. W. Lea (2004), Links between salinity variation in the Caribbean and North Atlantic thermohaline circulation, *Nature*, *428*, 160–163, doi:10.1038/nature02346.

Shackleton, N. J., and N. D. Opdyke (1973), Oxygen isotope and palaeomagnetic stratigraphy of equatorial Pacific core V28–238: Oxygen isotope temperatures and ice volumes on a 100 kyrs and 1000 kyrs scale, *Quat. Res.*, *3*(1), 39–54, doi:10.1016/0033-5894(73)90052-5.

Singer, B. S., H. Guillou, B. R. Jicha, C. Laj, C. Kissel, B. L. Beard, and C. M. Johnson (2009), $^{40}Ar/^{39}Ar$, K-Ar and ^{230}Th-^{238}U dating of the Laschamp excursion: A radioisotopic tie-point for ice core and climate chronologies, *Earth Planet. Sci. Lett.*, *286*(1–2), 80–88, doi:10.1016/j.epsl.2009.06.030.

Steinke, S., M. Mohtadi, J. Groeneveld, L.-C. Lin, L. Löwemark, M.-T. Chen, and R. Rendle-Bühring (2010), Reconstructing the southern South China Sea upper water column structure since the Last Glacial Maximum: Implications for the East Asian winter monsoon development, *Paleoceanography*, *25*, PA2219, doi:10.1029/2009PA001850.

Stott, L., C. Poulsen, S. Lund, and R. Thunell (2002), Super ENSO and global climate oscillations at millennial time scales, *Science*, *297*, 222–226, doi:10.1126/science.1071627.

Stott, L., K. Cannariato, R. Thunell, G. H. Haug, A. Koutavas, and S. Lund (2004), Decline of surface temperature and salinity in the western tropical Pacific Ocean in the Holocene epoch, *Nature*, *431*, 56–59, doi:10.1038/nature02903.

Stott, L., A. Timmermann, and R. Thunell (2007), Southern Hemisphere and deep-sea warming led deglacial atmospheric CO_2 rise and tropical warming, *Science*, *318*, 435–438, doi:10.1126/science.1143791.

Svensson, A., et al. (2008), A 60 000 year Greenland stratigraphic ice core chronology, *Clim. Past*, *4*, 47–57, doi:10.5194/cp-4-47-2008.

Széréméta, N., F. Bassinot, Y. Balut, L. Labeyrie, and M. Pagel (2004), Oversampling of sedimentary series collected by giant piston corer: Evidence and corrections based on 3.5-kHz chirp profiles, *Paleoceanography*, *19*, PA1005, doi:10.1029/2002PA000795.

Takahashi, T. (1959), Hydrographical researches in the western equatorial Pacific, *Mem. Fac. Fish. Kagoshima Univ.*, *7*, 141–147.

Thevenon, F., E. Bard, D. Williamson, and L. Beaufort (2004), A biomass burning record from the West Equatorial Pacific over the last 360 ky: Methodological, climatic and anthropic implications, *Palaeogeogr. Palaeoclimatol. Palaeoecol.*, *213*(1–2), 83–99, doi:10.1016/j.palaeo.2004.07.003.

Thunell, R. C., and L. A. Reynolds (1984), Sedimentation of planktonic foraminifera: Seasonal changes in species flux in the Panama Basin, *Micropaleontology*, *30*, 243–262, doi:10.2307/1485688.

Toole, J. M., R. C. Millard, Z. Wang, and S. Pu (1990), Observations of the Pacific North Equatorial Current Bifurcation at the Philippine Coast, *J. Phys. Oceanogr.*, *20*(2), 307–318, doi:10.1175/1520-0485(1990)020<0307:OOTPNE>2.0.CO;2.

Tozuka, T., T. Kagimoto, Y. Masumoto, and T. Yamagata (2002), Simulated multiscale variations in the western tropical Pacific: The Mindanao Dome revisited, *J. Phys. Oceanogr.*, *32*(5), 1338–1359, doi:10.1175/1520-0485(2002)032<1338:SMVITW>2.0.CO;2.

Udarbe-Walker, M. J. B., and C. L. Villanoy (2001), Structure of potential upwelling areas in the Philippines, *Deep Sea Res., Part I*, *48*(6), 1499–1518, doi:10.1016/S0967-0637(00)00100-X.

Visser, K., R. Thunell, and L. Stott (2003), Magnitude and timing of temperature change in the Indo-Pacific warm pool during deglaciation, *Nature*, *421*, 152–155, doi:10.1038/nature01297.

Waelbroeck, C., L. Labeyrie, E. Michel, J. C. Duplessy, J. F. McManus, K. Lambeck, E. Balbon, and M. Labracherie (2002), Sea-level and deep water temperature changes derived from benthic foraminifera isotopic records, *Quat. Sci. Rev.*, *21*(1–3), 295–305, doi:10.1016/S0277-3791(01)00101-9.

Wang, B., R. G. Wu, and X. H. Fu (2000), Pacific-East Asian teleconnection: How does ENSO affect East Asian climate?, *J. Clim.*, *13*(9), 1517–1536, doi:10.1175/1520-0442(2000)013<1517:PEATHD>2.0.CO;2.

Wang, B., I. S. Kang, and J. Y. Lee (2004), Ensemble simulations of Asian-Australian monsoon variability by 11 AGCMs, *J. Clim.*, *17*(4), 803–818, doi:10.1175/1520-0442(2004)017<0803:ESOAMV>2.0.CO;2.

Wijffels, S., E. Firing, and J. Toole (1995), The Mean Structure and Variability of the Mindanao Current at 8-Degrees-N, *J. Geophys. Res.*, *100*(C9), 18,421–18,435, doi:10.1029/95JC01347.

Xiang, R., Y. Sun, T. Li, D. W. Oppo, M. Chen, and F. Zheng (2007), Paleoenvironmental change in the middle Okinawa Trough since the last deglaciation: Evidence from the sedimentation rate and planktonic foraminiferal record, *Palaeogeogr. Palaeoclimatol. Palaeoecol.*, *243*, 378–393, doi:10.1016/j.palaeo.2006.08.016.

Xiao, J. L., Z. S. An, T. S. Liu, Y. Inouchi, H. Kumai, S. Yoshikawa, and Y. Kondo (1999), East Asian monsoon variation during the last 130,000 Years: Evidence from the Loess Plateau of central China and Lake Biwa of Japan, *Quat. Sci. Rev.*, *18*(1), 147–157, doi:10.1016/S0277-3791(97)00097-8.

Xu, J., W. Kuhnt, A. Holbourn, N. Andersen, and G. Bartoli (2006), Changes in the vertical profile of the Indonesian Throughflow during Termination II: Evidence from the Timor Sea, *Paleoceanography*, *21*, PA4202, doi:10.1029/2006PA001278.

Xu, J., W. Kuhnt, A. Holbourn, M. Regenberg, and N. Andersen (2010), Indo-Pacific Warm Pool variability during the Holocene and Last Glacial Maximum, *Paleoceanography*, *25*, PA4230, doi:10.1029/2010PA001934.

Yamagata, T., Y. Shibao, and S. Umatani (1985), Interannual Variability of the Kuroshio Extension and its relation to the Southern Oscillation/El Niño, *J. Oceanogr. Soc. Jpn*, *41*, 274–281, doi:10.1007/BF02109276.

Zhang, Y. G., J. Ji, W. L. Balsam, L. Liu, and J. Chen (2007), High resolution hematite and goethite records from ODP 1143, South China Sea: Co-evolution of monsoonal precipitation and El Niño over the past 600,000 years, *Earth Planet. Sci. Lett.*, *264*(1–2), 136–150, doi:10.1016/j.epsl.2007.09.022.

Zhang, Y. G., J. F. Ji, W. Balsam, L. W. Liu, and J. Chen (2009), Mid-Pliocene Asian monsoon intensification and the onset of Northern Hemisphere glaciation, *Geology*, *37*(7), 599–602, doi:10.1130/G25670A.1.

Zuraida, R., A. Holbourn, D. Nürnberg, W. Kuhnt, A. Dürkop, and A. Erichsen (2009), Evidence for Indonesian Throughflow slowdown during Heinrich events 3–5, *Paleoceanography*, *24*, PA2205, doi:10.1029/2008PA001653.

N. Andersen, Leibniz Laboratory for Radiometric Dating and Stable Isotope Research, Christian-Albrechts University, D-24118 Kiel, Germany.

L. Beaufort, CEREGE, Aix-Marseille Université, CNRS, IRD, Europôle Méditerranéen de l'Arbois, BP 80, F-13545 Aix-en-Provence, France.

T. Bolliet, D. Garbe-Schönberg, A. Holbourn, and W. Kuhnt, Institute of Geosciences, Christian-Albrechts University, Ludewig-Meyn-Str. 10-14, D-24118 Kiel, Germany. (ah@gpi.uni-kiel.de)

M. Kienast, Department of Oceanography, Dalhousie University, 1355 Oxford St., Halifax, NS B3H 4J1, Canada.

C. Kissel and C. Laj, Laboratoire des Sciences du Climat et de l'Environnement/IPSL, CEA/CNRS/UVSQ, Ave. de la Terrasse, F-91198 Gif-sur-Yvette CEDEX, France.